Journal of *Marine Science and Engineering*

MDPI

Article

Development of a Power Calculation Model of Hybrid-Sized Wave Energy Converter Arrays

Anru Fan [1], Huibo Zhang [1,*], Yijia Zhang [2], Junchen Liu [1] and Jinming Yao [3]

[1] College of Mechanical and Electrical Engineering, Harbin Engineering University, Harbin 150001, China; fananru@hrbeu.edu.cn (A.F.); liu_junchen@hrbeu.edu.cn (J.L.)
[2] School of Electrical Engineering, Tianjin Vocational College of Mechanics and Electricity, Tianjin 300000, China; Zhangdatigezi@163.com
[3] School of Astronautics, Harbin Institute of Technology, Harbin 150001, China; 22b318015@stu.hit.edu.cn
* Correspondence: zhanghuibo@hrbeu.edu.cn

Abstract: Because of its reliability, large reserves, and high safety standards, wave energy power generation has become an important part of the renewable energy industry. Hybrid-sized wave energy converter arrays consist of floats of different sizes. They have higher output power and stability and are the future development direction of wave power generation. However, the energy-absorbing floats in existing power calculation models are still in a traditional uniform-size configuration and cannot accurately calculate the energy generated by hybrid-sized wave energy converter arrays. In this paper, a time-domain power calculation model of hybrid-sized wave energy converter arrays is proposed. Based on linear wave theory, a frequency-domain hydrodynamic model is constructed and transformed into a time-domain model. The time-domain characteristics and influencing factors of wave energy converters are analyzed. Finally, a time-domain power calculation model of hybrid-sized wave energy converter arrays is established. Based on the irregular model setting and water entry conditions, an experimental verification study on the power calculation model is carried out using the wave energy converter previously developed by the research team. The results show that the average error of the power calculation model proposed in this paper is less than 10%, demonstrating the accuracy of the model.

Keywords: wave energy power generation; hybrid-sized array; hydrodynamic modeling; power calculation model

check for updates

Academic Editor: Eugen Rusu

Received: 24 January 2025
Revised: 19 February 2025
Accepted: 25 February 2025
Published: 27 February 2025

Citation: Fan, A.; Zhang, H.; Zhang, Y.; Liu, J.; Yao, J. Development of a Power Calculation Model of Hybrid-Sized Wave Energy Converter Arrays. *J. Mar. Sci. Eng.* **2025**, *13*, 460. https://doi.org/10.3390/jmse13030460

Copyright: © 2025 by the authors. Licensee MDPI, Basel, Switzerland. This article is an open access article distributed under the terms and conditions of the Creative Commons Attribution (CC BY) license (https://creativecommons.org/licenses/by/4.0/).

1. Introduction

Marine energy is clean energy, which is helpful for addressing current problems such as energy shortages and environmental pollution. Various types of marine energy have abundant reserves, among which wave energy has received widespread attention due to its high energy density, wide distribution range, and low mining difficulty. There are many arrangements for wave energy converters. Among these, arranging wave energy converters in an array can significantly improve the collection of wave energy [1]. With the advancement of research in related fields in recent years, Giassi discovered the following: compared with traditional wave-energy array configurations with the same float sizes, forming a hybrid-sized wave energy power generation array with floats of different sizes can further improve the output power of the array [2]. Configuration changes in hybrid-sized wave energy converter arrays (hereafter referred to as "hybrid arrays") are more diverse, so configuration optimization can effectively increase power and enhance utilization. The most critical aspect is the construction of a power calculation model.

In the field of power model construction, Sinha et al. studied the power generation performance of five different point-suction wave energy converter arrays under different incident wave directions [3]. Giassi M et al. carried out a study on the layout optimization of large-size wave energy converter arrays, considering factors such as the length of transmission cables and the distance between each device and the transmission node. The results showed that even when considering economic costs, the power calculation model of the wave energy converter array remained the most important factor affecting array optimization [4]. Kara expanded the frequency-domain model calculation tool ITU-WAVE based on the time-varying boundary integration method to calculate the impact of vertical walls on wave energy absorption in wave energy converter arrays when the distance is small [5]. Li used traditional frequency-domain models to calculate the hydrodynamic parameters of large-scale wave energy converter arrays. Li et al. proposed a physically constrained Gaussian model to address the problem of excessive computational cost [6]. The frequency-domain hydrodynamic models constructed for existing wave energy converter arrays are based on traditional array configurations with uniform float sizes and do not consider differences in frequency-domain response calculations for hybrid arrays, which may make the power calculation results inaccurate.

Based on the fixed size model and further considering the application of different sizes, Goteman et al. conducted a study on the parameters that affect the energy harvesting effect of the hybrid array. They found that the array arranged in a semicircle exhibited fewer fluctuations in the energy harvesting power of the float than the array arranged in a rectangle. In addition, the study included a simple optimization scheme for the layout of the hybrid array [7]. Sun accounted for irregular wave conditions. She analyzed the impact of different float shapes on the energy harvesting effect of hybrid arrays and found that float size and mass had the greatest influence. The research provided a simple optimization scheme for the mass and size of the float [8]. Abdulkadir et al. studied float-size arrays and hybrid-sized arrays with the same total float mass. They compared the power generation performance of wave energy power systems and used genetic algorithms to optimize the float shape and layout [9]. Current research on power generation efficiency uses the energy captured by the float as the output power of the array but does not consider possible power losses from captured energy to output energy, nor does it consider differences in losses caused by floats of different sizes.

To sum up, in existing research on hybrid arrays, the power calculation method used for hybrid arrays is the same as the traditional calculation method for arrays with the same-size configuration, and no power calculation model suitable for hybrid-sized arrays has been established. In addition, existing studies regard the captured energy power of the float as the output power of the array, which cannot directly reflect the generated power of the array in the time domain. As a result, when research is based on existing models, the calculated results cannot accurately reflect the power generation performance of the array. Therefore, to study the power of hybrid-sized wave power arrays and provide a more accurate calculation method, it is necessary to build a time-domain power calculation model (hereafter referred to as the "time-domain model") for hybrid-sized wave power arrays.

2. Methods

2.1. Modeling of Fluid Dynamics

Linear wave theory is the fundamental theory in potential flow theory. In this section, based on regular incident waves with a single incident direction, the hydrodynamic model of a mixed-size wave energy array in the frequency domain is established.

In the application of linear wave theory, the following six assumptions are made: the influence of fluid viscosity is not considered; the fluid is powerful and non-rotating; the

density of the fluid is constant and cannot be compressed; the free surface pressure of the fluid is equal to atmospheric pressure; the wave height of a wave is much smaller than its wavelength; and the seabed is a solid boundary and cannot be crossed.

Under linear wave theory, the change in the wave surface can be expressed by the following equation:

$$\eta = H_{am}\cos(nx - \omega t) \tag{1}$$

In the formula, H_{am} is the amplitude, which is equal to half the wave height; n is the wave number; ω is the angular frequency of the wave, which satisfies $\omega^2 = gn\tanh(nh_{sea})$; g is the acceleration due to gravity; and h_{sea} is the water depth.

In frequency-domain modeling of mixed-size wave power generation arrays, the difference between the mixed-size array and the traditional array configurations is not considered, which leads to inaccurate calculation results. Therefore, this section examines the construction of a frequency-domain hydrodynamic model for mixed-size wave power generation arrays.

In order to address this problem accurately, we only study the energy-absorbing floats and their array configuration, rather than the entire power generation device.

Assuming that the array has a total of $N+1$ floats, the floating platform is numbered 0, and the remaining floats are numbered 1 to N. Each float is connected to the floating platform through an oscillating float-type wave energy converter, as shown in Figure 1. Each float is determined by its radius R^i, draft d^i, and position (x^i, y^i, z^i), where i is the number of the float and its values are 1 to N. $z = 0$ is the hydrostatic balance surface in the vertical direction of the coordinate system. $z = -h_{sea}$ is the seabed. The cylindrical coordinate system (r, θ, ζ) is defined with the position coordinates of each float as the origin. The coordinates of any point on the float surface can be expressed as follows in the local coordinate system: $(x, y, z) = (x^i + R^i\cos\theta, y^i + R^i\sin\theta, z^i + \xi)$. Note that for each floating body, the basin is divided into two parts. The area below the floating body, where the diameter is smaller than that of the floating body, is called the inner area, while the area with a larger diameter is called the outer area, as shown in Figure 1. The fluid areas are divided accordingly.

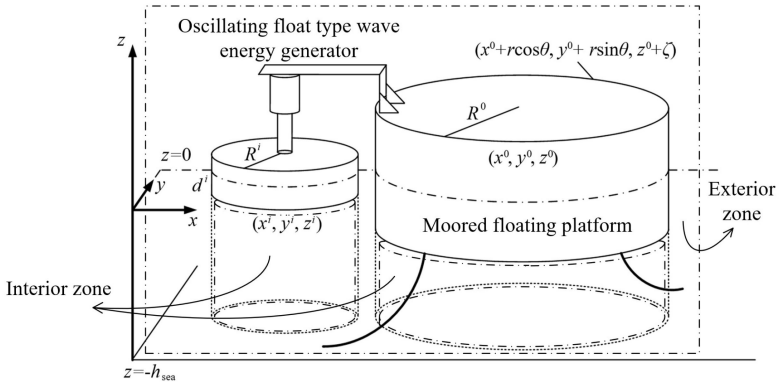


Figure 1. Diagram of the coordinate system for the array of a hybrid-sized wave energy converter.

Based on linear potential flow theory, the total velocity potential of a wave can be decomposed into the incident potential, scattering potential, and radiation potential. When solving the scattering problem, it is necessary to assume that all floats are fixed, and when solving the radiation problem, it is essential to rely on the scattering potential solution results without incident waves.

The motion of the fluid in the flow field is continuous, and its velocity potential function satisfies the two-dimensional Laplace equation:

$$\Delta\phi = \frac{\partial^2\phi}{\partial x^2} + \frac{\partial^2\phi}{\partial z^2} \tag{2}$$

where Δ is the Laplace operator.

In linear wave theory, the wave motion in the vertical direction is regarded as a small amplitude vibration, so the boundary condition at the wave free surface can be simplified as

$$\left.\frac{\partial\phi}{\partial z}\right|_{z=\eta} = \frac{\partial\eta}{\partial t} \tag{3}$$

The hydrodynamic boundary conditions at the surface are

$$\eta = -\frac{1}{g}\left.\frac{\partial\phi}{\partial t}\right|_{z=\eta} \tag{4}$$

where g is the acceleration due to gravity.

Since Equations (3) and (4) also hold true on a still water surface, applying Taylor's formula, we have

$$\left.\frac{\partial\phi}{\partial z}\right|_{z=0} = \frac{\partial\eta}{\partial t} \tag{5}$$

$$\eta = -\frac{1}{g}\left.\frac{\partial\phi}{\partial t}\right|_{z=0} \tag{6}$$

Combining the above two equations, we have

$$\left.\left(\frac{\partial\phi}{\partial z} + \frac{1}{g}\frac{\partial^2\phi}{\partial t^2}\right)\right|_{z=0} = 0 \tag{7}$$

Since the seabed boundary is horizontal and cannot be crossed, the fluid particles have no vertical velocity component at the bottom surface, so the boundary condition at the seabed is

$$u_z|_{z=-h_{sea}} = \left.\frac{\partial\phi}{\partial z}\right|_{z=-h_{sea}} = 0 \tag{8}$$

In summary, the wave boundary condition under linear wave conditions is shown in Formula (9):

$$\begin{cases} \Delta\phi = \dfrac{\partial^2\phi}{\partial x^2} + \dfrac{\partial^2\phi}{\partial z^2} = 0 \\ \eta = -\dfrac{1}{g}\left.\dfrac{\partial\phi}{\partial t}\right|_{z=0} \\ \left.\left(\dfrac{\partial\phi}{\partial z} + \dfrac{1}{g}\dfrac{\partial^2\phi}{\partial t^2}\right)\right|_{z=0} = 0 \\ u_z|_{z=-h_{sea}} = \left.\dfrac{\partial\phi}{\partial z}\right|_{z=-h_{sea}} = 0 \end{cases} \tag{9}$$

Given the wave angular frequency and wave number, the above boundary problem can be solved by the method of undetermined coefficients to obtain the velocity potential function of the wave. Combining the wave surface Equation (1) with the free surface boundary condition (6) yields

$$\phi|_{z=0} = \frac{gH_{am}}{\omega}\sin(nx - \omega t) \tag{10}$$

Since the fluctuation amplitude of the fluid below the water surface decreases with increasing depth, the amplitude H_{am} can be regarded as a function of the water depth. Since ω is a given value, the velocity potential function can be expressed by the following formula:

$$\phi(x,z,t) = H_{am}(z)\sin(nx-\omega t) \tag{11}$$

Combining the above equation with Equation (2), we have

$$\left[H_{am}''(z) - n^2 H_{am}(z)\right]\sin(nx-\omega t) = 0 \tag{12}$$

Formula (12) is a second-order homogeneous linear differential equation with constant coefficients, and its general solution can be written as

$$H_{am}(z) = H_{am1}e^{nz} + H_{am2}e^{-nz} \tag{13}$$

where H_{am1} and H_{am2} are coefficients to be determined.

Associating Equation (13) with the free water surface motion condition (6) and the seabed boundary condition (8) yields

$$\begin{cases} H_{am1} = \dfrac{gH_{am}e^{nh_{sea}}}{2\omega\cosh(nh_{sea})} \\ H_{am2} = \dfrac{gH_{am}e^{-nh_{sea}}}{2\omega\cosh(nh_{sea})} \end{cases} \tag{14}$$

Therefore, the velocity potential of linear waves under given conditions can be expressed as

$$\phi = \frac{gH_{am}}{\omega}\frac{\cosh(nz+nh_{sea})}{\cosh(nh_{sea})}\sin(nx-\omega t) \tag{15}$$

Simultaneously solving the wave-front Equation (6) and the velocity potential expression (15) gives the wave-front equation in the propagation process:

$$\eta(x,y,t) = -\frac{1}{g}\frac{\partial\phi}{\partial t}\bigg|_{z=0} = H_{am}\cos(nx-\omega t) \tag{16}$$

Using the Fourier transform, the velocity potential function can be transformed into the frequency domain, and using the Bessel function matrix, the incident wave matrix acting on float i can be expressed in the local coordinate system of float i as

$$\phi^i_{0,k}(x) = \sum_{k=-\infty}^{\infty} Z_0(z)A^i_{0k}J_k(nr)e^{ik\theta} \tag{17}$$

where $Z_0(z)$ is the vertical component of the velocity potential function, A^i_{0k} is the incident wave coefficient matrix, $J_k(nr)$ is the Bessel function matrix, and r is the radius used to characterize the external area. When $r > R^i$, the sea area is an external area, and vice versa. The vertical function and incident wave coefficient can be obtained from Equation (18) and Equation (19), respectively,

$$Z_0(z) = \frac{1}{N_0}\cosh(nz+nh_{sea}), N_0^2 = \frac{1}{2}(1+\frac{\sinh(2nh_{sea})}{2nh_{sea}}) \tag{18}$$

$$A^i_{0,k} = -\frac{igA^i(\omega)}{\omega}\frac{1}{Z_0(0)}e^{inx^i i^k} \tag{19}$$

Define the basin below the floating body as an internal area and the other basins as an external area. The general scattered waves in the external region can be represented by

the matrix of the propagation Hankel function $H_k(nr)$ and the matrix of the evanescent modified Bessel function $K_k(n_m r)$ [10]:

$$\phi_S^{i(out)} = \sum_{k=-\infty}^{\infty} \left[\alpha_{0k}{}^i Z_0(z) \frac{H_k(nr)}{H_k(nR^i)} + \sum_{m=1}^{\infty} \alpha_{mk}{}^i Z_m(z) \frac{K_k(n_m r)}{K_k(n_m R^i)} \right] e^{ik\theta} \tag{20}$$

In the formula, the frequency equation under the wave number n_m satisfies $\omega^2 = -g n_m \tanh(n_m h_{sea})$. $Z_m(z)$ can be determined using Formula (21):

$$Z_m(z) = \frac{1}{N_m} \cosh(n_m z + n_m h_{sea}), N_m^2 = \frac{1}{2}(1 + \frac{\sinh(2n_m h_{sea})}{2n_m h_{sea}}) \tag{21}$$

According to the addition theorem of the Bessel function, in an array composed of several floating bodies, the scattered wave of floating body j can be expressed as the incident wave on another floating body i in its local coordinate system. Therefore, the total diffraction waves in the outer area of floating body i consist of the scattered wave $\phi_S^{i(out)}$ of floating body i itself, the incident wave $\phi_{0,k}^i$ from infinity, and the incident wave $\sum_{j \neq i} \phi_S^{i(out)}\Big|_i$ generated by the scattering of floating bodies other than the floating body, as shown in Formula (22):

$$\begin{aligned} \phi_D^{i(out)} &= \phi_{0,k}^i + \phi_S^{i(out)} + \sum_{j \neq i} \phi_S^{i(out)}\Big|_i \\ &= \sum_{k=-\infty}^{\infty} \left[Z_0(z)(\alpha_{0k}^i \frac{H_k(nr)}{H_k(nR^i)} + J_k(nr)(A_{0,n}^i + \sum_{j \neq i} \sum_{l=-\infty}^{\infty} T_{0lk}^{ij} \alpha_{0l}^j)) \right. \\ &\left. + \sum_{m=1}^{\infty} Z_m(z)(\alpha_{mk}^i) \frac{K_k(n_m r)}{K_k(n_m R^i)} + \frac{I_k(n_m r)}{I_k(n_m R^i)} \sum_{j \neq i} \sum_{l=-\infty}^{\infty} T_{mlk}^{ij} \alpha_{ml}^j \right] e^{ik\theta} \end{aligned} \tag{22}$$

where T_{0lk}^{ij} and T_{mlk}^{ij} can be determined by Formulas (23) and (24), and $I_k(n_m r)$ is a modified Bessel matrix.

$$T_{0lk}^{ij} = \frac{1}{H_l(nR^j)} H_{l-k}(nR_{ij}) e^{i\theta_{ij}(l-k)} \tag{23}$$

$$T_{mlk}^{ij} = \frac{I_n(n_m R^i)}{K_l(n_m R^j)} K_{l-k}(n_m R_{ij}) e^{i\theta_{ij}(l-k)} (-1)^k \tag{24}$$

The potential function of the inner region, that is, the basin below the cylinder, is given by

$$\phi_D^{i(in)} = \sum_{k=-\infty}^{\infty} \sum_{m=0}^{\infty} \gamma_{mk}^i \frac{I_k(\lambda_m^i r)}{I_k(\lambda_m^i R^i)} \cos(\lambda_m^i (z + h_{sea})) e^{ik\theta} \tag{25}$$

where $\lambda_m^i = \pi m / L^i$, L^i is the distance from the bottom of floating body i to the seabed, given by $L^i = h_{sea} - d^i$. γ_{mk}^i can be determined by Formula (26), where s and k need to be substituted into the obtained variables.

$$\gamma_{sk}^i = \sum_{m=0}^{\infty} (\alpha_{mn}^i + J_k(nR^i) A_{0,n}^i + J_k(nR^i) \sum_{j \neq i} \sum_{l=-\infty}^{\infty} T_{mlk}^{ij} \alpha_{ml}^j) c_{sm}^i \tag{26}$$

Then, we have $c_{sm}^i = (-1)^s n_m \sin(n_m L^i) / (n_m^2 - \lambda_s^i) L^i N_m$.

In order to solve for the potential flow factor α in the scattering potential, based on the fact that the derivative of the fluid potential at the boundary of the domain is also continuous, some parameters in the potential flow also satisfy the following two equations:

$$\sum_{m=0}^{\infty} \left[\tilde{D}_{smk}^i d_{smk}^i - \tilde{L}_{smk}^i (\alpha_{mk}^i + J_k(nR^i) \sum_{j \neq i} \sum_{l=-\infty}^{\infty} T_{mlk}^{ij} \alpha_{ml}^j) \right] = Q_{sam} \tag{27}$$

$$Q_{sam} = \tilde{L}^i_{s0k} J_k(nR^i) A^i_{0,n} \tag{28}$$

Then, we have $\tilde{D}^i_{smk} = \tilde{q}^i_{mk} - \tilde{\tilde{L}}^i_{smk} J_k(nR^i)$ and $\tilde{\tilde{L}}^i_{smk} = 2\sum_{r=0}^{\infty} \tilde{\tilde{P}}^i_{rk} c^i_{rm} c^i_{rs}$. Because this paper adopts a closed-cylinder float [10], $\tilde{\tilde{P}}^i_{rk} = 0$. q^i_{mk} can be calculated by Formula (29):

$$\tilde{q}^i_{mk} = h_{sea} \frac{d}{dr} \left(\frac{I_k(n_m r)}{I_k(n_m R^i)} \right) \Big|_{r=R^i} \tag{29}$$

Based on Formula (27), by truncating the infinite matrix and adopting a semi-analytical method, α^i_{mk} and d^i_{mk} can be obtained. Add the truncated angle to $\sum_n e^{ik\theta}$ and the vertical velocity to $\sum_m Z_m(z)$ by using Sum_θ and Sum_z. When $Sum_z \geq 1$, it shows that the calculation of waves is evanescent, and when $Sum_z = 0$, scattered waves are equivalent to plane waves or behave as if they are at a sufficiently large distance. According to the research results of Mclver [11], the plane wave approximation in the water area with a radius of 4–8 times that of the floating body can stably produce results with obvious differences that are not easily confused. Therefore, the arrangement spacing of floats in this section is 3–10 times the radius.

To sum up, the scattering potential flow factor matrix α can be solved by the following matrix:

$$\begin{bmatrix} U & -B^1_M T^{12} & \cdots & -B^1_M T^{1N} \\ -B^2_M T^{21} & U & \cdots & -B^2_M T^{2N} \\ \vdots & \vdots & \ddots & \vdots \\ -B^N_M T^{N1} & -B^N_M T^{N1} & \cdots & U \end{bmatrix} \begin{bmatrix} \alpha^1 \\ \alpha^2 \\ \vdots \\ \alpha^N \end{bmatrix} = \begin{bmatrix} B^1_{dir} \\ B^2_{dir} \\ \vdots \\ B^N_{dir} \end{bmatrix} \tag{30}$$

$$B^i_M = -\left[D^i - (\hat{L}\tilde{\tilde{D}}^{-1}\tilde{L})^i \right]^{-1} \left[\tilde{D}^i - (\hat{L}\tilde{\tilde{D}}^{-1}\tilde{\tilde{L}})^i J_k(nr) \right] \tag{31}$$

$$B^i_{dir} = B^i_M A^i_{0,k} \tag{32}$$

Similarly, since the floating bodies used in this paper are all closed cylinders, Equation (31) can be simplified as follows:

$$B^i_M = -{D^i_{smk}}^{-1} \tilde{D}^i_{smk} \tag{33}$$

where $D^i_{smk} = q^i_{mk} - L^i_{smk}$ and $\tilde{D}^i_{smk} = \tilde{q}^i_{mk} - \tilde{L}^i_{smk} J_k(nR^i)$. q^i_{mk}can be obtained from Formula (34), L^i_{smk} and $\tilde{L}^i_{smk}$ are given by $L^i_{smk} = \sum_{r=0}^{\infty} \left[\varepsilon_n L^i dR^i_{mk}(r)|_{r=R^i} \right] / dr$ and $\tilde{L}^i_{smk} = 0$. Here, ε_n is the Neumann symbol, where 1 is taken when the wave number $n = 0$, and 2 is taken when it is not equal to 0. $\tilde{q}^i_{mk}$ can be obtained from Formula (35):

$$q^i_{mk} = h_{sea} \frac{d}{dr} \left(\frac{K_k(n_m r)}{K_k(n_m R^i)} \right) \Big|_{r=R^i} \tag{34}$$

$$\tilde{q}^i_{mk} = h_{sea} \frac{d}{dr} \left(\frac{H_k(n_m r)}{H_k(n_m R^i)} \right) \Big|_{r=R^i} \tag{35}$$

The square on the left side of Equation (30) is $N(Sum_z + 1)(2Sum_\theta + 1)$. The size of identity matrix U and each matrix element $B^i_M T^{ij}$ is $(Sum_z + 1)(2Sum_\theta + 1)$.

Göteman et al. proposed a method through their research. Under the condition that a certain error is allowed, according to the characteristics of the array, a limiting action distance can be selected to restrict the hydrodynamic action range between any two floats, and the floats beyond this range do not affect each other. When the number of floats in the array is large, this method can significantly improve computational efficiency [12].

Based on the calculation of multiple scattering potentials in the above-mentioned paper, the expressions of the scattering potentials in the inner region and the outer region

can be obtained, which satisfy the boundary conditions of the seabed, floating body, and free sea surface; have no incident wave; and consider the scattering and radiation effects at the same time, as shown in Equations (36) and (38), respectively,

$$\phi_D^{i(in)} = \frac{V^i}{2L^i}\left((z+h_{sea})^2 - \frac{r^2}{2}\right)U + \sum_{k=-\infty}^{\infty}\sum_{m=0}^{\infty}\beta_{mk}^i R_{mk}^i(r)\cos(\lambda_m^i(z+h_{sea}))e^{ik\theta} \quad (36)$$

In the formula, β_{mk}^i can be obtained from Formula (37):

$$\beta_{mk}^i = V^i L^i\left[\left(\frac{R^i}{2L^i}\right)^2 - \frac{1}{6}\right]U + \sum_{m=0}^{\infty}(\tilde{\alpha}_{mk}^i + J_k(nR^i)\sum_{j\neq i}\sum_{l=-\infty}^{\infty}T_{mlk}^{ij}\tilde{\alpha}_{ml}^j)c_{sm}^i \quad (37)$$

When calculating the external region, for the floating body, the "incident wave", which is involved in the calculation, is equivalent to the sum of the scattered waves and radiation waves from the other floating bodies in the array. The overall diffraction potential should be the sum of the scattering potential, radiation potential, and "incident potential".

$$\begin{aligned}\phi_D^{i(out)} &= \phi_R^{i(out)} + \phi_S^{i(out)} + \sum_{j\neq i}\left[\phi_R^{j(out)} + \phi_S^{j(out)}\right] \\ &= \sum_{k=-\infty}^{\infty} e^{ik\theta}\left[Z_0(z)\left(\tilde{\alpha}_{0k}^i\frac{H_k(nr)}{H_k(nR^i)} + J_k(nr)\sum_{j\neq i}\sum_{l=-\infty}^{\infty}T_{0lk}^{ij}\tilde{\alpha}_{0l}^j\right)\right. \\ &\left. + \sum_{m=1}^{\infty}Z_m(z)\left(\tilde{\alpha}_{mk}^i\frac{K_k(n_m r)}{K_k(n_m R^i)} + \frac{I_k(n_m r)}{I_k(n_m R^i)}\sum_{j\neq i}\sum_{l=-\infty}^{\infty}T_{mlk}^{ij}\tilde{\alpha}_{ml}^j\right)\right]\end{aligned} \quad (38)$$

The potential flow factor $\tilde{\alpha}_{mk}^i = \alpha_{mk}^i + V^i b_{mk}^i$. The calculation method is the same as that in the previous section. Because the derivative of the fluid potential at the boundary of the domain is also continuous, some parameters in the potential flow satisfy the following two equations, from which $\tilde{B}_R^i$ can be obtained using Equation (41):

$$\sum_{m=0}^{\infty}\left[\tilde{D}_{smk}^i f_{mk}^i - \tilde{L}_{smk}^i(\tilde{\alpha}_{mk}^i + J_k\left(nR^i\right)\sum_{j\neq i}\sum_{l=-\infty}^{\infty}T_{mlk}^{ij}\alpha_{ml}^j\right] = R_{sam} \quad (39)$$

$$R_{sam} = V^i\tilde{B}_R^i \quad (40)$$

$$\begin{aligned}\tilde{B}_R^i = &-\frac{1}{2}UR^i c_{os}^i + 2L^i c_{0s}^i(\tilde{P}_{0k}^i((\frac{R^i}{2L^i})^2 - \frac{1}{6}) \\ &- \frac{1}{6}\tilde{P}_{0k}^i) - 2L^i\sum_{m=1}^{\infty}(\tilde{P}_{mk}^i + \tilde{P}_{mk}^i)c_{ms}^i\frac{(-1)^m}{\pi^2 m^2}\end{aligned} \quad (41)$$

In this formula, $\tilde{p}_{mk}^i = \tilde{p}_{mk}^i = \varepsilon_n L^i dR_{mk}^i(r)/2dr\big|_{r=R^i}$. Let $m = 0$; then, $\tilde{p}_{mk}^i$ and $\tilde{p}_{0k}^i$ can be obtained.

$$\begin{bmatrix} U & -B_M^1T^{12} & \cdots & -B_M^1T^{1N} \\ -B_M^2T^{21} & U & \cdots & -B_M^2T^{2N} \\ \vdots & \vdots & \ddots & \vdots \\ -B_M^NT^{N1} & -B_M^NT^{N2} & \cdots & U \end{bmatrix}\begin{bmatrix}\tilde{\alpha}^1 \\ \tilde{\alpha}^2 \\ \vdots \\ \tilde{\alpha}^N\end{bmatrix} = \begin{bmatrix}V^1B_{rad}^1 \\ V^2B_{rad}^2 \\ \vdots \\ V^2B_{rad}^2\end{bmatrix} \quad (42)$$

$$B_{rad}^i = -{D_{smk}^i}^{-1}\tilde{B}_R^i \quad (43)$$

where B_{rad}^i can be obtained using Formula (43). Except for the potential flow factor, the other elements are the same as those in the solution matrix of the scattering potential flow factor in Equation (30). After the potential flow factor $\tilde{\alpha}^i$ is obtained using the above formula, f_{mk}^i can be obtained using Formulas (39) and (40). Then, β_{mk}^i in Formula (37) can be obtained to solve Equation (36).

In the previous calculation, the scattering potential function and radiation potential function associated with floating body I in the array can be obtained using the multiple scattering equation and the multiple radiation equation of the array, after which the excitation force and radiation force of floating body I can be obtained by integration.

The surface of the floating body is discretized based on the parametric element discretization method satisfying Green's function [13]. For the whole basin, under the condition that the boundary conditions shown in Equation (9) are satisfied, the internal and external basin potential functions, which are obtained in the above two sections, all have both the second and first derivatives at the boundary. Therefore, Green's function is used to calculate the velocity potential. The wave velocity potential function satisfying Equation (9) can be calculated using integration under the mixed distribution model [14], and the calculation formula is shown in Equation (44):

$$4\pi\phi^i(p) = \iint_S \left[G\frac{\partial \phi^i}{\partial n_z} + \phi^i \frac{\partial G}{\partial n_z} \right] ds \tag{44}$$

The Green's function in infinite water depth and the Green's function in limited water depth are shown in Equation (45) and Equation (46), respectively:

$$G = \frac{w + w_1}{w w_1} + \frac{V^i}{\pi} \int_L \frac{2e^{n(z+\zeta)}}{n - V^i} J_0(nR^i) dn \tag{45}$$

$$G = \frac{w + w_2}{w w_2} + \int_L \frac{2(n + V^i)\cosh(z + h_{sea})\cosh n(z + \zeta)}{n\sinh(nh_{sea}) - V^i \cosh(nh_{sea})} J_0(nR^i) dn \tag{46}$$

In the above two formulas, w, w_1, and w_2 are Green's function water depth condition operators, which can be solved by Formulas (47) to (49):

$$w = (x - r\cos\theta)^2 + (y - r\sin\theta)^2 + (z - \zeta)^2 \tag{47}$$

$$w_1 = (x - r\cos\theta)^2 + (y - r\sin\theta)^2 + (z + \zeta)^2 \tag{48}$$

$$w_2 = (x - r\cos\theta)^2 + (y - r\sin\theta)^2 + (z + \zeta + 2h_{sea})^2 \tag{49}$$

When integrating the mixed-size wave energy converter array with Green's function, calculations must be based on the draft parameters of each floating body and the water depth of its basin. In this section, the water depth correction function $f_m(d^i)$ is introduced to modify the Green's function calculation formula, and the modified Green's function expression is given in Formula (50):

$$\begin{aligned} G_m = {} & \frac{1}{w} + \frac{f_m(d^i)}{w_1} + \frac{f_m(d^i)}{w_2} + 2J_0(nR^i) \int_L \left[\frac{f_m(d^i) V^i e^{n(z+\zeta)}}{\pi(n - V^i)} \right. \\ & \left. + \frac{(n + V^i)\cosh(z + h_{sea})\cosh n(z + \zeta)}{n\sinh(nh_{sea}) - V^i\cosh(nh_{sea})} f_m(d^i) \right] dn \end{aligned} \tag{50}$$

The expression of the water depth correction function $f_m(d^i)$ is shown in Formula (51), where τ_h is the water depth condition discriminant factor, which satisfies the relation $\tau_h = e, (h_{sea} \geq 9d^i)$; $\tau_h = 1, (h_{sea} < 9d^i)$.

$$f_m(d^i) = \frac{h_{sea} - 9d^i}{|h_{sea} - 9d^i|} + \ln \tau_h \tag{51}$$

In this way, the correction is completed. The hydrodynamic parameters of floats in mixed-size arrays can be calculated by integration based on Equation (50).

The hydrodynamic parameters are solved as described below.

The modified Green's function is used to solve the excitation force and radiation force of each float in the array, and the excitation force and radiation force of the float in the array are shown in Formula (52) and Formula (53), respectively:

$$\begin{aligned} F_{Ex}^{i} &= i\omega\rho \iint_{S_b} r dr \phi_D^{i(in)}(r,\theta,-d^i) \\ &= 2\pi i\omega\rho \left[\gamma_{00}^{i} \frac{(R^i)^2}{2} + 2\sum_{m=1}^{\infty} (-1)^m \gamma_{m0}^{i} \int_0^{R^i} r dr \frac{I_0(\lambda_m^i r)}{I_0(\lambda_m^i R^i)} \right] \end{aligned} \tag{52}$$

The potential flow function in the above formula is the potential flow function of the internal river basin under the multiple scattered waves obtained in Formula (25).

$$\begin{aligned} F_{Ra}^{i} &= i\omega\rho \iint_{S_b} r dr \phi_D^{i(in)}(r,\theta,-d^i) \\ &= 2\pi i\omega\rho \left[f_{v1} + a_{00}^{i} \frac{(R^i)^2}{2} \right] + 2\sum_{m=1}^{\infty} (-1)^m a_{m0}^{i} \int_0^{R^i} r dr \frac{I_0(\lambda_m^i r)}{I_0(\lambda_m^i R^i)} \end{aligned} \tag{53}$$

The potential flow function in the above formula is the potential flow function of the internal basin under the multiple radiation waves obtained in Formula (36), where f_{v1} is the radiation force velocity and depth operator, which can be obtained using Formula (54):

$$f_{v1} = \left[V^i L^i \left((R^i L^i)^2 - (R^i)^4 \right) \right] / 16 (L^i)^2 \tag{54}$$

In the calculation of multiple radiation potentials, there is a relationship between the potential flow factor and the heave velocity, as shown in Formula (26) [10]:

$$\tilde{\alpha}^i = \left[DIM^{-1} \right]_i^i V^i B_{rad}^i + \sum_{j \neq i} \left[DIM^{-1} \right]_j^i V^j B_{rad}^i \tag{55}$$

To sum up, the heave speed of all floats can be determined from the calculation of the radiation force. The off-diagonal elements in the diffraction matrix represent the radiation force between different floats, and the radiation force is usually divided into two parts, namely $F_{Ra}^i = -m_{add}\ddot{z} - B\dot{z}$. In the frequency domain, it can be expressed by Formula (56), where m_{add} is the added mass and B is the radiation damping:

$$F_{Ra}^i = \left[i\omega m_{add} - B \right]_i^i V^i + \sum_{j \neq i} \left[i\omega m_{add} - B \right]_j^i V^j \tag{56}$$

The multiple radiation problem and the multiple scattering problem can be solved independently of each other. They can also be solved together when there are incident waves and each float can move freely in the vertical direction. The solution method is the same as that mentioned above, and the potential flow factor includes both scattered and radiated waves; that is, the right part of Equation (42) is multiplied by the right part of Equation (30).

After calculating the excitation force and radiation force of each float using Formulas (52) and (53), the response equation of the float in the frequency domain can be obtained by giving the frequency and wave number of the incident wave. Assuming that the connection between the float and the wave power generation device is rigid, that is, they have the same displacement in the vertical direction, and the mooring floating platform is regarded as static in the horizontal direction and only pendulous in the vertical

direction, the response equation of the float in the frequency domain can be written as follows [15]:

$$F_{Ex}^{i} = \left[-\omega^2(m^i + m_{add}^i(\omega)) - i\omega B^i(\omega) - \rho g S_{ae}\right] z^i(\omega) \quad (57)$$

where m^i is the total mass, including the float and wave power generation device; S_{ae} is the water section area of the float; and $z^i(\omega)$ is the vertical motion amplitude response operator of the float, that is, the RAO (Response Amplitude Operator) operator.

When the potential flow theory is used to calculate the frequency response of the float, the influence of the viscous effect is usually ignored. However, in the mixed-size wave energy converter array, because the sizes of the floats that make up the array are different, it is necessary to determine whether the viscous effect is significant for the relatively small floating bodies in the array and to modify the calculation accordingly. In this section, a correction factor for the floating body viscous effect is given to distinguish the relatively small floating bodies in the array, and its frequency-domain response equation is corrected.

When a relatively small cylindrical float is subjected to waves, the excitation force term in the frequency-domain response equation is less affected by the viscous effect, while the radiation damping term and the additional mass term are greatly affected by the viscous effect [16], so the viscous effect of a relatively small floating body cannot be ignored in the calculation.

Wu Shuang et al. [17] tried to solve the problem that, under the potential flow theory, the viscous effect cannot be ignored in the frequency-domain response calculation of floating bodies, and the modified coefficient functions of added mass and radiation damping were given by the McQuart least square method in the way of data fitting. The maximum errors between the fitted added mass and radiation damping and the original data were 1.9% and 3.6%, respectively. Although the error was within the allowable range, the fitting method used in the fitting process paid too much attention to matching the dataset, resulting in overfitting. Moreover, the quality of the fitted function graph was not good, and no examples were provided to verify the effectiveness of the fitting function.

Neural networks have strong nonlinear fitting capabilities and good generalization ability. To address the overfitting problem in the fitting process, the Bayesian regularization method can be used for improvement. Therefore, in this section, the Bayesian regularization method is used to train the neural network, and the data obtained from its references are re-fitted to solve the problems existing in the viscosity correction coefficient function. The modified frequency-domain response equation is shown in Equation (58):

$$z^i(\omega) = \frac{F_{Ex}^{i}}{-\omega^2(m^i + m_{add}^i(\omega) f_{ad}) - i\omega B^i(\omega) f_{dp} - \rho g S_{ae}} \quad (58)$$

where f_{ad} is the additional mass correction factor and f_{dp} is the radiation damping correction factor.

In this section, the fitting model of the neural network is built, and 80% of the data obtained from the references are used as training data. The verification data and test data are each set to 10%, and the number of layers of the neural network is set to four. Under the training of the Bayesian regularization method, the fitting functions of the neural network to additional mass and radiation damping are shown in Figure 2 and Figure 3, respectively. Compared with the original document image, the overfitting phenomenon of the modified coefficient function image after re-fitting is significantly reduced, and the image quality is significantly improved. At the same time, 10% of the data is reserved for the verification of the fitting model, which makes the model more accurate. The maximum error of the modified additional mass correction coefficient model is 0.78%, and the maximum error of the radiation damping correction coefficient model is 1.96%, both of which are better than

the references. In the follow-up research in this section, the obtained model is used to build the simulation model in the neural network module in Python. The training framework of the Bayesian regularization method is shown in Formula (59):

$$P(x_p|D_{trn}, \alpha_{nro}, \beta_{nro}, M_{mdl}) = e^{-F(xp)} / Z_F(\alpha_{nro}, \beta_{nro}) \quad (59)$$

In the formula, $Z_F(\alpha_{nro}, \beta_{nro}) = (\pi/\alpha_{nro})^4 (\pi/\beta_{nro})^4$ and $F(x_p) = \beta_{nro} E_D + \alpha_{nro} E_W$.

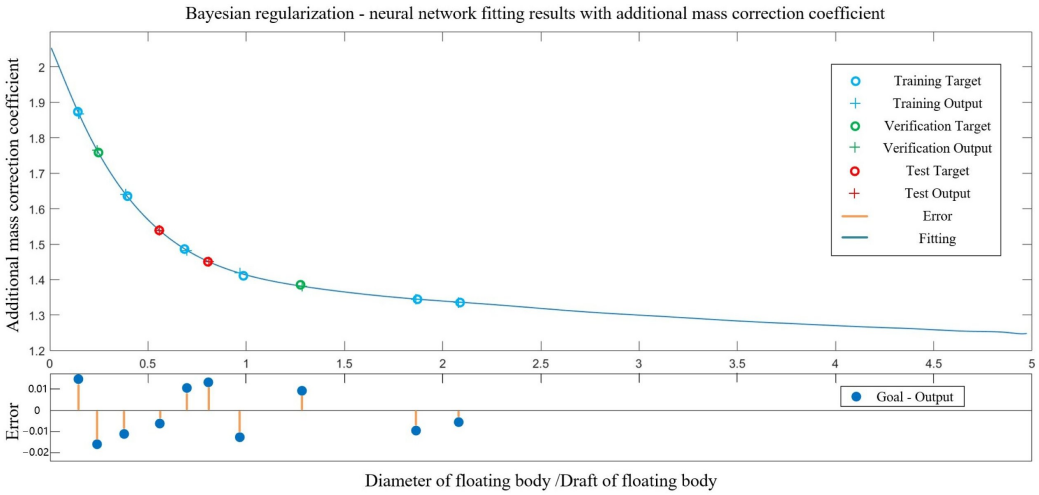


Figure 2. Added mass correction coefficient re-fitting results.

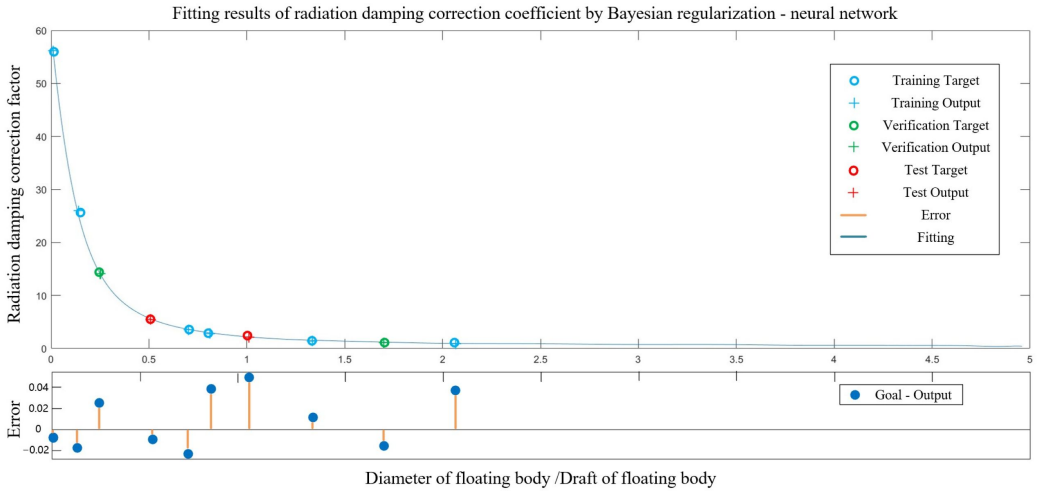


Figure 3. Radiation damping correction coefficient re-fitting results.

The fitted neural network with the additional mass correction coefficient and radiation damping correction coefficient satisfies $F_1(x_p)$ and $F_2(x_p)$, respectively, as shown in Equations (60) and (61):

$$F_1(x_p) = 0.000549\beta_{nro1} + 22.0709\alpha_{nro1} \quad (60)$$

$$F_2(x_p) = 0.006528\beta_{nro2} + 4556.59\alpha_{nro2} \quad (61)$$

In the formula, $\alpha_{nro1}/\beta_{nro1} = 0.0114$ and $\alpha_{nro2}/\beta_{nro2} = 0.0153$.

Determining whether a floating body is a relatively small floating body mainly depends on whether the overall diameter of the floating body is greater than 0.2 times the wave wavelength in the flow field. Considering the viscous effect of relatively small floating

bodies in the array, the frequency-domain response correction equation of each floating body in the array can be expressed by Equation (62):

$$z^i(\omega) = \frac{F_{Ex}^i}{-\omega^2(m^i + m_{add}^i(\omega)\xi_1) - i\omega B^i(\omega)\xi_2 - \rho g S_{ae}} \tag{62}$$

$$\xi_1 = \begin{cases} f_{ad}, R^i \le 5n/\pi \\ 1, R^i > 5n/\pi \end{cases} \tag{63}$$

$$\xi_2 = \begin{cases} f_{dp}, R^i \le 5n/\pi \\ 1, R^i > 5n/\pi \end{cases} \tag{64}$$

In the formula, ξ_1 and ξ_2 are the correction factors for the added mass and radiation damping viscous effect, respectively.

Based on the above contents, the frequency-domain response simulation model of a floating body with a hybrid-sized wave energy converter array is built, and the effectiveness of the frequency-domain calculation model is verified through a simulation verification model.

Using Python, this paper builds a simulation verification model for the formula derived above. The simulation results are compared with those of the hydrodynamic simulation to verify the advantages of the improved frequency-domain response model over the existing model. The specific parameters of each floating body in the simulation model are shown in Table 1, and the simulation model is shown in Figure 4.

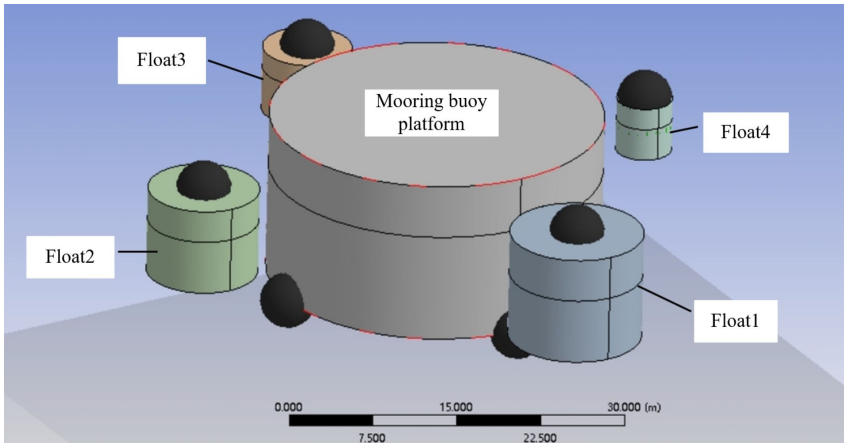


Figure 4. Hydrodynamic simulation model.

Table 1. Parameters of the floating bodies in the simulation model.

Project	Size (Diameter × Draft)
Dimensions of mooring floating platform	30 m × 10 m (limited water depth)
Float 1	12 m × 6 m (limited water depth)
Float 2	10 m × 5 m (limited water depth)
Float 3	8 m × 4 m (infinite water depth)
Float 4	5 m × 3 m (infinite water depth)
Depth of water	45 m

The improved model proposed in this paper accurately calculates the frequency-domain response of mixed-size wave energy converter arrays when the viscous effect of relatively small floating bodies cannot be ignored. For a floating body in the array, whether its influence due to viscous effect can be ignored under the action of waves is mainly

determined by the relationship between its diameter and wave number in the wave field. Based on the above simulation model, the calculation accuracy of the modified model is verified through three conditions: a large wave number, a medium wave number, and a wavelet number.

As shown in Figure 5, the frequency-domain responses of the four floats in the simulation model under different calculation models are compared, and the selected wave number is $n = 0.24\ \mathrm{m}^{-1}$. Under the large wave number condition, Float 1, Float 2, and Float 3 were all less affected by the viscous effect, and only Float 4 was greatly affected. It can be clearly seen in the figure that there was little difference between the modified calculation model and the unmodified model in the frequency-domain response calculation of Float 1, Float 2, and Float 3, and they all fit well with the verification model. However, due to the failure to fully consider the influence of the viscous effect, the uncorrected model exhibited obvious deviations in the frequency-domain response calculation of Float 4. In contrast, the modified model in this paper still fit well with the verification model. It should be noted that, as shown in Figure 5c, although Float 3 was less affected by the viscous effect, there was still some deviation in the calculation results of the uncorrected model, and the response exhibited a shift in the high-frequency direction in the high-frequency band. This is due to the inaccurate calculation of the wave force integral in the frequency domain by the uncorrected model. The modified model is based on the water depth condition of Green's function, and the wave force integral is corrected, allowing it to fit the verification model well. The high-frequency shift in the calculation of the frequency-domain response of Float 4 in the uncorrected model was the same as described above.

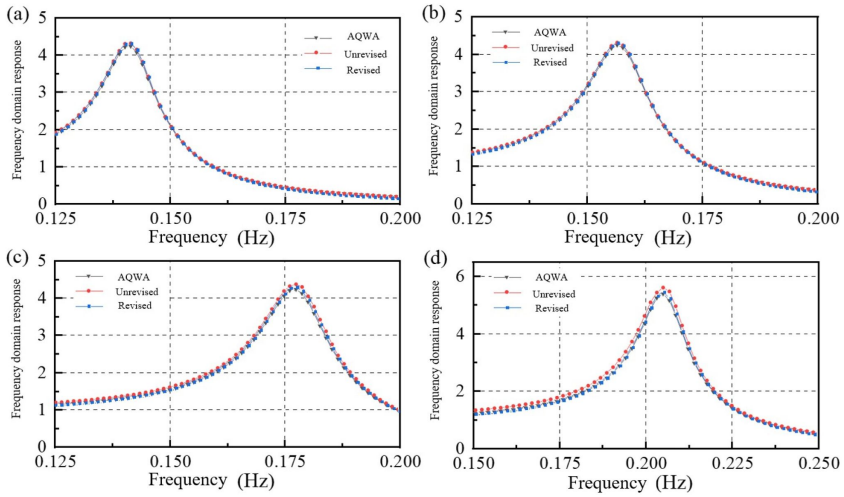


Figure 5. Frequency-domain responses of four floats by different computational models under the high wave number condition: (**a**) Float 1; (**b**) Float 2; (**c**) Float 3; (**d**) Float 4.

As shown in Figure 6, the frequency-domain responses of the four floats in the simulation model under different calculation models are compared, and the selected wave number is $n = 0.12\ \mathrm{m}^{-1}$. Under the medium wave number condition, except for Float 1, the other three floats were greatly affected by the viscous effect. As can be seen in the figure, when the uncorrected model was used to calculate the frequency-domain responses of Floats 2, 3, and 4, there were significant deviations, and the smaller the size of the calculated floats, the greater the deviation. At the same time, the frequency-domain responses of Floats 3 and 4 calculated by the uncorrected model still exhibited obvious deviations in the high-frequency band. It should be noted, however, that although the high-frequency shift of the two floats was obviously larger than that in the large wave number condition shown in Figure 6, theoretically, the high-frequency shift in the frequency-domain response calculation was independent of the wave number. Considering that the calculation distor-

tion caused by the viscous effect was not fully considered, it increases as the wave number decreases, and the high-frequency shift in the frequency-domain response calculation of Floats 3 and 4 was likely caused by the increased deviation in the frequency-domain response due to the viscous effect. In contrast, the modified model in this paper exhibited better agreement with the frequency-domain response calculations of the four floats and the verification model.

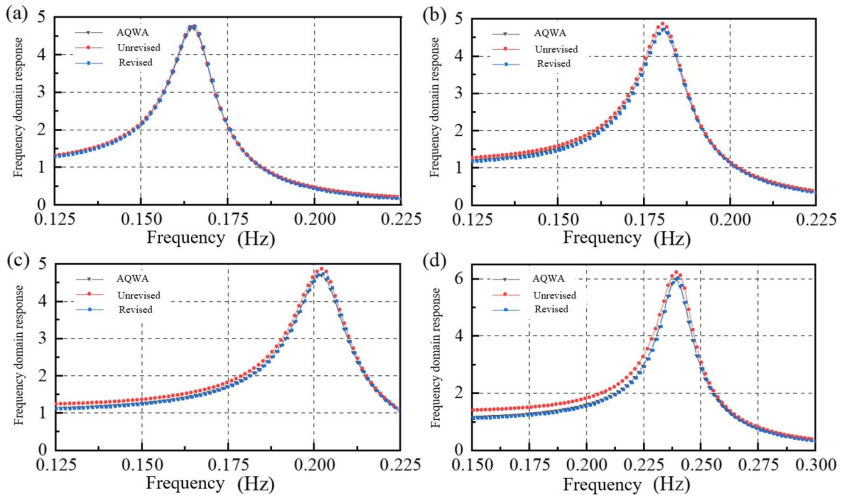


Figure 6. Frequency-domain responses of four floats by different computational models under the middle wave number condition: (**a**) Float 1; (**b**) Float 2; (**c**) Float 3; (**d**) Float 4.

As shown in Figure 7, the frequency-domain responses of the four floats in the simulation model under different calculation models are compared, and the selected wave number is $n = 0.06\ \mathrm{m}^{-1}$. Under the wavelet number condition, all the floats in the simulation model were affected by the viscous effect. In the figure, it can be seen that the uncorrected model exhibited varying degrees of deviation in the frequency-domain response calculations of all the floats, and the smaller the float, the greater the deviation. As shown in Figure 7d, the calculation results of the original model deviated significantly from those of the verification model. However, the modified model in this paper exhibited better agreement with the frequency-domain response calculations of the four floats and the verification model. The high-frequency band shift and the increase in the offset in the calculation of the uncorrected model were analyzed and discussed in relation to Figures 5 and 6 in the previous section and are not repeated here.

To sum up, the uncorrected frequency-domain response calculation model of mixed-size wave energy array floats exhibits increasing deviation in calculation results as the wave number decreases, and the smaller the calculated float size, the more obvious the deviation. At the same time, high-frequency response deviation occurs in the frequency-domain calculation of some relatively small floats in the array.

Table 2 shows the maximum errors of the uncorrected and corrected models under three wave number conditions. The maximum error of the modified model was smaller than that of the unmodified model across different wave numbers, and it was not affected by changes in the wave number. Based on the analysis of the frequency-domain response calculation results before and after correction under three wave numbers, it can be seen that the frequency-domain response calculation results of the modified model in this paper are better than those of the unmodified model under the large wave number, medium wave number, and wavelet number conditions.

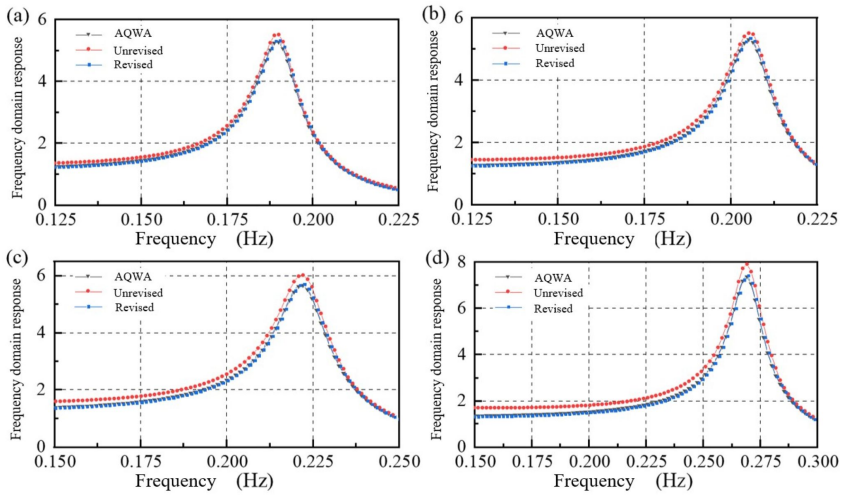


Figure 7. Frequency-domain responses of four floats by different computational models under the wavelet number condition: (**a**) Float 1; (**b**) Float 2; (**c**) Float 3; (**d**) Float 4.

Table 2. The maximum error of the uncorrected and corrected models under three different wave number conditions.

Wave Condition	Maximum Deviation of Uncorrected Model	Maximum Deviation of Modified Model
Large wave number	3.62%	0.84%
Medium wave number	6.78%	1.03%
Wavelet number	11.26%	0.95%

In this section, the wave velocity potential, multiple scattering potential, and multiple radiation potential of the wave field are modeled, and the boundary integral equation and frequency-domain response equation of a floating body are modified, providing a basis for the subsequent establishment of the time-domain power calculation model.

2.2. Time-Domain Power Calculation Model of Hybrid Array

2.2.1. Wave Power Generation Device Design

Based on the wave conditions in most sea areas, an oscillating float-type wave energy converter was designed and developed, with the PTO system and motor modeled in the time domain. In this section, an oscillating float-type wave energy converter is designed using a ball screw as the core mechanical component of the PTO system. The three-dimensional design of the device is shown in Figure 8.

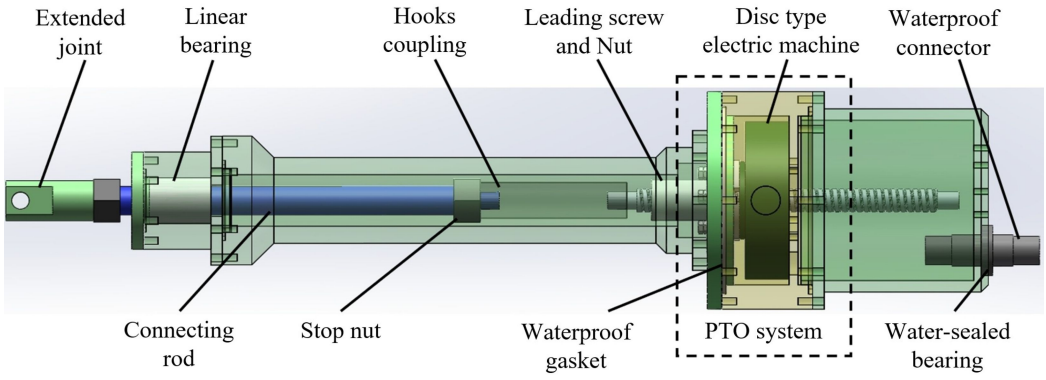


Figure 8. Structure of oscillating float-type wave energy converter.

The device features a disk-type hollow motor, and the screw support adopts a linear bearing–screw nut configuration, which greatly reduces the size of the device and improves its application value without affecting performance. The expansion joint at the front end is connected to the wave-absorbing float through an expansion component. The wave energy absorbed by the float is transmitted to the screw through the linear motion of the connecting rod, which, in turn, drives the nut connected to the motor to rotate, driving the motor to generate electrical energy, realizing wave energy conversion to electrical energy. Waterproof washers are installed between each shell of the device, and the extended part of the connecting rod blocks the seawater through an external waterproof sleeve.

After completing the overall design of the oscillating float-type wave energy converter, in order to conduct dynamic modeling of the PTO system, the specific application scenarios of the device need to be designed. The wave energy converter designed in this paper is part of a hybrid-sized wave energy generation array. Its application schematic is shown in Figure 1. Through the vertical oscillation of the float, the motion generated by waves is directly transmitted to the connecting rod of the conversion device, driving the motor to rotate and generate electricity.

In this application scenario, the PTO system of the oscillating float-type wave power generation device designed in this paper is a linear system, which is equivalent to a spring–mass damping system in the vertical direction [18], as shown in Figure 9.

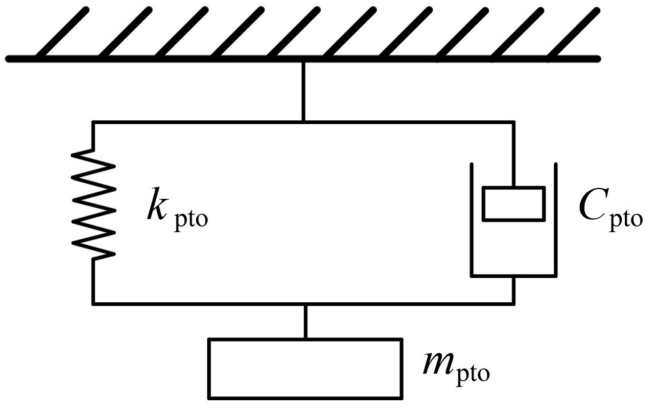


Figure 9. Equivalent diagram of wave power converter PTO system under heave motion.

The PTO force is shown in the following formula, where m^i_{pto} is the mass of the PTO system and C^i_{pto} is the equivalent damping of the PTO system:

$$F^i_{PTO}(t) = m^i_{pto}\ddot{z}^i(t) + C^i_{pto}\dot{z}^i(t) \tag{65}$$

A ball screw has the advantages of low friction resistance and high transmission efficiency, and the size of the wave power generation device can be significantly reduced by combining it with a disc motor. In the process of converting the linear reciprocating motion of the float into the rotary motion of the motor, the axial force and torque on the lead screw satisfy Equation (66), and the rotary motion of the lead screw satisfies Equation (67).

$$F^i_{ax}(t) = 2\pi T^i_{ax}(t)/l^i_{\text{le}}\eta^i_{tr} \tag{66}$$

where $F^i_{ax}(t)$ is the axial force of the screw, $T^i_{ax}(t)$ is the screw torque, η^i_{tr} is the transmission efficiency, and l^i_{le} is the lead of the screw.

$$\omega^i_{sc}(t) = 2\pi v^i_{sc}/l^i_{\text{le}} \tag{67}$$

where $\omega_{sc}^{i}(t)$ is the angular velocity of the screw nut rotation and v_{sc}^{i} is the linear motion speed of the ball screw in the axial direction.

When the motor is rotating to generate electricity, there is a generator load torque $T_{ge}^{i}(t)$, and its value is directly proportional to the speed of the generator, which can be expressed by Formula (68):

$$T_{ge}^{i}(t) = K_{tr}^{i} K_{el}^{i} \omega_{ge}^{i}(t) / (R_{inr}^{i} + R_{etr}^{i}) \tag{68}$$

where K_{tr}^{i} and K_{el}^{i} are the generator torque constant and electrical constant, respectively; R_{inr}^{i} and R_{etr}^{i} are the internal resistance and load resistance, respectively; and $\omega_{ge}^{i}(t)$ is the rotation angular velocity of the generator, with its value the same as the rotation angular velocity of the nut $\omega_{sc}^{i}(t)$.

The torque of the whole wave power generation device satisfies Equation (69):

$$T_{ax}^{i}(t) - T_{ge}^{i}(t) = (J_{ax}^{i} + J_{ge}^{i}) \dot{\omega}_{ge}^{i}(t) \tag{69}$$

where J_{ax}^{i} is the moment of inertia of the lead screw nut and J_{ge}^{i} is the moment of inertia of the disc motor.

Therefore, the expression of the PTO force, obtained from Equations (66) to (69), is

$$F_{PTO}^{i}(t) = (J_{ax}^{i} + J_{ge}^{i}) \frac{4\pi^2}{(l_{le}^{i})^2 \eta_{tr}^{i}} \ddot{z}^{i}(t) + \frac{K_{tr}^{i} K_{el}^{i}}{(R_{inr}^{i} + R_{etr}^{i})} \frac{4\pi^2}{(l_{le}^{i})^2 \eta_{tr}^{i}} \dot{z}^{i}(t) \tag{70}$$

Combined with Formula (65), the mass and damping of the PTO system can be expressed by the following formula:

$$m_{pto}^{i} = \frac{4\pi^2 (J_{ax}^{i} + J_{ge}^{i})}{(l_{le}^{i})^2 \eta_{tr}^{i}}, C_{pto}^{i} = \frac{4\pi^2 K_{tr}^{i} K_{el}^{i}}{(R_{inr}^{i} + R_{etr}^{i})(l_{le}^{i})^2 \eta_{tr}^{i}} \tag{71}$$

Based on Equations (70) and (71), a relatively complete dynamic model of the PTO system can be constructed.

2.2.2. Power Calculation Model Model

In Section 2.2.1, the dynamic modeling of the PTO system was carried out. In order to obtain the output electric power of the power generation device and supplement the dynamic modeling of the PTO system based on electromagnetic torque, it is necessary to model the motor. In this paper, the disc-type permanent magnet synchronous motor is used, so this section derives the mathematical model for calculating the output power of the permanent magnet synchronous motor. First, the following assumptions are made [19]: (1) the induced electromotive forces of the three-phase lines of the stator winding are sine waves, and they are symmetrically distributed; (2) the rotor damping and eddy current effects of the generator are not considered; and (3) the influence of temperature is ignored.

Under the above assumptions, the wave pushes the float to make a vertical motion and then drives the rotor of the motor to rotate and cut the magnetic induction line to generate electric energy. The induced electromotive forces of the three phases of the motor are shown in Formulas (72) to (74), respectively:

$$E_a = d\psi_a / dt = -\psi_{ev} \omega_{ev} \sin\theta_m \tag{72}$$

$$E_b = d\psi_b / dt = -\psi_{ev} \omega_{ev} \sin(\theta_m - 2\pi/3) \tag{73}$$

$$E_c = d\psi_c / dt = -\psi_{ev} \omega_{ev} \sin(\theta_m + 2\pi/3) \tag{74}$$

where E_a, E_b, and E_c are the induced electromotive forces of the three phases of the permanent magnet motor a, b, and c, respectively; ω_{ev} is the electrical angular velocity of the permanent magnet motor rotor; ψ_{ev} is the magnetic linkage of the rotor permanent magnet; and θ_m is the rotor position angle.

According to the law of loop voltage, the relationship between the phase voltage and electromotive force of a permanent magnet synchronous motor is as follows:

$$E_x = L_{inx}(di_x/dt) + i_x R_{sa} + U_x \tag{75}$$

where E_x is the electromotive force of phase x(a or b or c), L_{inx} is the inductance of phase x, i_x is the current of phase x, R_{sa} is the internal resistance of the motor stator, and U_x is the stator end output of phase x.

Based on Equations (72) to (75), the stator terminal voltage equations for a permanent magnet motor are given by

$$U_a = -i_a R_{sa} - L_{ina}(di_a/dt) + (d\psi_a/dt) \tag{76}$$

$$U_b = -i_b R_{sa} - L_{inb}(di_b/dt) + (d\psi_b/dt) \tag{77}$$

$$U_c = -i_c R_{sa} - L_{inc}(di_c/dt) + (d\psi_c/dt) \tag{78}$$

From a basic knowledge of electricity, it is known that the single-phase output power of a permanent magnet synchronous motor is given by

$$P_{ot} = U_x^2/R_{loadx} \tag{79}$$

where P_{ot} is the single-phase output power of the permanent magnet motor and R_{loadx} is the resistance value of the single-phase load of the permanent magnet motor.

In order to calculate the electromagnetic torque of the permanent magnet synchronous motor used in this paper, it is necessary to transform the phase coordinates of its voltage. First, the established model needs to be converted from a three-phase coordinate system to a two-phase coordinate system; that is, a Clarke transformation from a static coordinate system to a dynamic coordinate system is applied, as shown in Figure 10a. Axis A, axis B, and axis C are the axes of the three-phase stator winding of the permanent magnet synchronous motor, while axis α and axis β are the axes of the converted two-phase static coordinate system. It should be noted that under the Clarke transformation, the A-axis and the α-axis coincide.

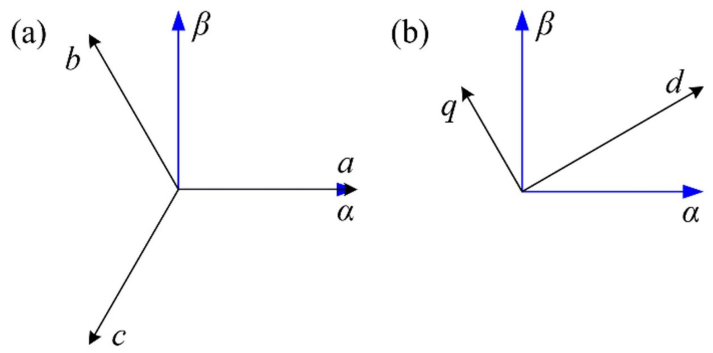


Figure 10. Permanent magnet synchronous motor coordinate transformation: (**a**) Clarke transformation; (**b**) Park transformation.

The Clarke transformation matrix for voltage is given in Formula (80), where u_α and u_β are the voltages in the two-phase coordinate system, and u_a, u_b, and u_c are the voltages in the three-phase coordinate system:

$$\begin{bmatrix} u_\alpha \\ u_\beta \end{bmatrix} = \sqrt{\frac{2}{3}} \begin{bmatrix} 1 & -\frac{1}{2} & -\frac{1}{2} \\ 0 & \frac{\sqrt{3}}{2} & -\frac{\sqrt{3}}{2} \end{bmatrix} \begin{bmatrix} u_a \\ u_b \\ u_c \end{bmatrix} \tag{80}$$

In order to convert the static two-phase coordinate system of the permanent magnet synchronous motor into the rotating two-phase dynamic coordinate system, it is necessary to apply a Park transformation to the coordinates, as shown in Figure 10b. The d-axis and q-axis of the rotating coordinate system are fixed to the rotor, and the Park transformation matrix for voltage is given in Formula (81):

$$\begin{bmatrix} u_d \\ u_q \end{bmatrix} = \begin{bmatrix} \cos\theta & \sin\theta \\ -\sin\theta & \cos\theta \end{bmatrix} \begin{bmatrix} u_\alpha \\ u_\beta \end{bmatrix} \tag{81}$$

where θ is the angle between the d-axis of the rotating coordinate system and the α-axis of the stationary coordinate system, and u_d and u_q are the voltages along the d-axis and q-axis, respectively, in the rotating coordinate system. By combining (80) and (81), the Park transformation matrix in the coordinate system is given in (82):

$$\begin{bmatrix} u_d \\ u_q \end{bmatrix} = \sqrt{\frac{2}{3}} \begin{bmatrix} \cos\theta & \cos(\theta - \frac{2\pi}{3}) & \cos(\theta + \frac{2\pi}{3}) \\ -\sin\theta & -\sin(\theta - \frac{2\pi}{3}) & -\sin(\theta + \frac{2\pi}{3}) \end{bmatrix} \begin{bmatrix} u_a \\ u_b \\ u_c \end{bmatrix} \tag{82}$$

Combining Equations (76) to (78), the voltages along the two axes in the two-phase rotating coordinate system are obtained as follows:

$$u_d = -R_{sa} i_d - \omega_{ev} L_{inq} i_q + L_{ind}(di_d/dt) \tag{83}$$

$$u_q = -R_{sa} i_q - \omega_{ev} L_{ind} i_d + L_{inq}(di_q/dt) + \omega_{ev} \psi_{ev} \tag{84}$$

In the formula, i_d and i_q represent the stator currents along the d-axis and q-axis, respectively, and L_{ind} and L_{inq} are the stator inductances along the d-axis and q-axis, respectively.

Therefore, the expression for the electromagnetic torque of the permanent magnet synchronous motor in the two-phase rotating coordinate system is given in Formula (85):

$$T_e = \frac{3}{2} n_r \left[\psi_{ev} i_q + (L_{ind} - L_{inq}) i_d i_q \right] \tag{85}$$

where n_r is the motor speed.

2.2.3. Time-Domain Transformation of Frequency-Domain Model

Based on the frequency-domain response equation of a mixed-size wave energy array, Equation (62) is transformed using the inverse Fourier transform, and then the PTO force on the floats in the time domain is introduced to obtain the motion response equation of each floating body, as shown in Equation (86).

$$F_{Ex}^i(t) = (m^i + m_{a\infty}^i)\dot{z}^i(t) + \int_{-\infty}^{t} K(t - \tau_m)\dot{z}^i(\tau_m) d\tau_m + \rho g S_{ae}^i z^i(t) - F_{PTO}^i(t) \tag{86}$$

where $F^i_{Ex}(t)$ is the wave excitation force on the float in the time domain, $K(t-\tau_m)$ is the hysteresis function matrix, $m^i_{a\infty}$ is the added mass of the float at an infinite wave frequency, τ_m is the time shift of the convolution term of the radiation force and excitation force based on linear time-invariant system theory, and $F^i_{PTO}(t)$ is the time-domain PTO force of the system.

In this paper, the fourth-order Runge–Kutta numerical integration method is used to solve the time-domain motion of floating bodies iteratively [14].

$$Q\left[t, z^i(t), \dot{z}^i(t)\right] = \left[F^i_{Ex}(t) - \int_{-\infty}^{t} K(t-\tau_m)\dot{z}^i(\tau_m)d\tau_m - \rho g S^i_{ae} z^i(t) + F^i_{PTO}(t)\right] / (m^i + m^i_{a\infty}) \tag{87}$$

When the fourth-order Runge–Kutta method is used to solve the problem, the displacement and velocity of the floating body are expressed as

$$z^i(t+\Delta t) = z^i(t) + \Delta t \cdot \dot{z}^i(t) + \Delta t \cdot (Q_1 + Q_2 + Q_3)/6 \tag{88}$$

$$\dot{z}^i(t+\Delta t) = \dot{z}^i(t) + (Q_1 + 2Q_2 + 2Q_3 + Q_4)/6 \tag{89}$$

The definitions of Q_1, Q_2, Q_3, and Q_4 are given in Formulas (90) to (93):

$$Q_1 = \Delta t \cdot Q\left[t, z^i(t), \dot{z}^i(t)\right] \tag{90}$$

$$Q_2 = \Delta t \cdot Q\left[t + \frac{\Delta t}{2}, z^i(t) + \frac{\Delta t \cdot \dot{z}^i(t)}{2}, \dot{z}^i(t) + \frac{Q_1}{2}\right] \tag{91}$$

$$Q_3 = \Delta t \cdot Q\left[t + \frac{\Delta t}{2}, z^i(t) + \frac{\Delta t \cdot \dot{z}^i(t)}{2} + \frac{\Delta t \cdot Q_1}{4}, \dot{z}^i(t) + \frac{Q_2}{2}\right] \tag{92}$$

$$Q_4 = \Delta t \cdot Q\left[t + \Delta t, z^i(t) + \Delta t \cdot \dot{z}^i(t) + \frac{\Delta t \cdot Q_2}{2}, \dot{z}^i(t) + Q_3\right] \tag{93}$$

Based on the displacement and velocity of the object at time t, the results of Q_1, Q_2, Q_3, and Q_4 can be computed. Then, based on the displacement and speed of the object at this time, the motion state of the object at the next time step can be calculated. Through this iterative calculation, the time-domain motion response of the floating body can be obtained.

2.2.4. Construction of Calculation Modules for Power Calculation Model

Based on the theoretical derivation carried out in the previous section, this section builds a time-domain response model for the float of a hybrid array in Python. The general concept of the model is shown in Figure 11.

Based on the frequency-domain response model of the float obtained in Section 2.1, it is transformed into a time-domain model using the inverse Fourier transform. Then, based on the PTO dynamics calculation model in the time domain and the electromagnetic torque calculation in the motor model above, the response calculation model of the float in the time domain can finally be obtained. The response calculation model is input into the power calculation model of the permanent magnet synchronous motor, and finally, the power calculation model of the hybrid array under the action of irregular waves in the time domain is obtained. At the same time, through the power model calculation module, interference is reduced and calculation efficiency is improved.

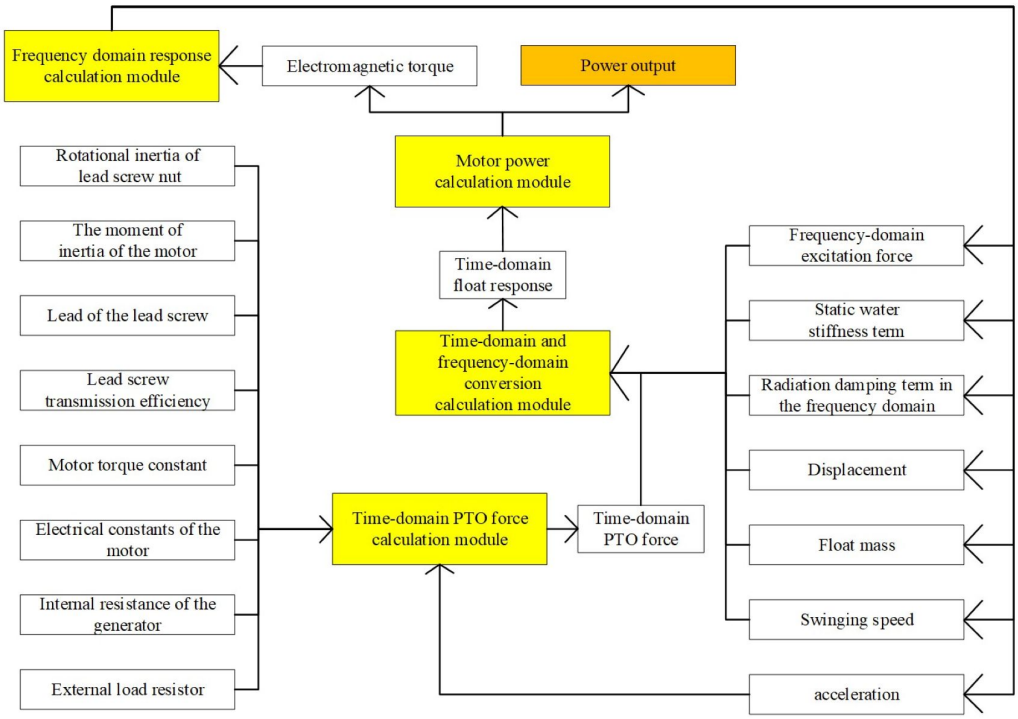


Figure 11. Operational modules of power calculation model.

3. Experimental Verification of Power Calculation Models

3.1. Verification of Parameter Settings

3.1.1. Experimental Equipment Construction

This section verifies the accuracy of the time-domain model. It was necessary to generate irregular incident waves through the established Jonswap spectrum, and then obtain the frequency-domain response of each float in the hybrid array under the action of irregular waves, based on the frequency-domain calculation model established previously. Then, the displacement and velocity of each float were obtained based on the PTO system dynamic model, motor model, and converted time-domain model established previously. Since the total output power of the array was a simple sum of the output power of the power generation devices connected to each float, if the output power corresponding to a single float was calculated accurately, it could be inferred that this model was also suitable for the calculation of the output power of the entire array. Because a single float can represent the effect of the whole array, in order to simplify the data analysis, this paper only analyzed the error curve of the theoretical and experimental data from the float with the largest error. At the end of this article, the error of the whole array is explained.

In this paper, a test prototype was made based on the oscillating float-type wave energy converter designed in Section 2.2.1, and a ground equivalent test (hereafter referred to as a "ground test") was designed for verification. The overall layout of the ground test is shown in Figure 12. Test equipment, such as prototypes and electric push rods, was installed on the optical platform. From the point of view of energy, the loss between mechanical energy and electric energy is large, while the loss from wave energy to mechanical energy is small. Therefore, the experimental device only considers the mechanical energy conversion part, the wave input is equivalent to the push rod movement, and the device is then designed.

The test used a PC as the upper computer, and the communication PLC, which controlled the electric push rod, simulated the motion input of the float to the wave energy converter under the action of irregular waves. The three-phase current output by the motor was rectified and connected to the external load. An oscilloscope was used to measure and

store the voltage on the external load and its waveform, and the electric power of the power generation device was calculated. The experimental prototype and the motor assembly used are shown in Figure 13.

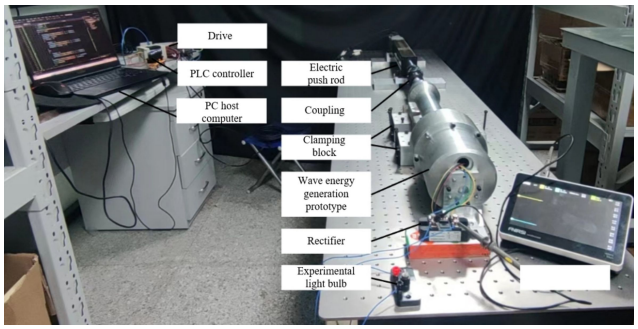


Figure 12. Layout of the ground test.

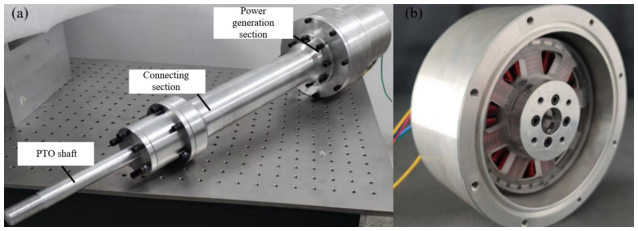


Figure 13. Experimental prototype: (**a**) Entire experimental prototype; (**b**) Disc motor assembly.

3.1.2. Incident Water Flow Setting

In order to realize a more practical simulation, it is critical to set the incident water flow. By referring to the actual marine environment, an irregular wave model is established to define the incident water flow conditions.

In the actual marine environment, the wave frequency of ocean waves is random, so when verifying the time-domain model, it is necessary to establish a spectrum model of irregular waves to provide the wave frequency for the frequency-domain response calculation equation in Section 2.2, and the core of establishing irregular waves is to simulate their spectrum. Suppose the frequency range of waves is divided into intervals, and the frequency difference of each interval is $\Delta\omega = (\omega_i - \omega_{i-1})$, then

$$\omega_i = (\omega_i + \omega_{i-1})/2 \tag{94}$$

By superposing all cosine waves in the divided interval, the wave-front equation shown in the following formula is obtained:

$$\eta(t) = \sum_{i=1}^{M} \cos(nx - \omega_i t)\sqrt{2S(\omega_i)\Delta\omega_i} \tag{95}$$

where ω_i is the wave frequency of the ith interval among M intervals and the difference between the frequencies of each interval is $\Delta\omega_i = (\omega_i + \omega_{i-1})M^{-1}$. Because the value of the interval division number m is too small, the wave action at the peak of the spectrum becomes too large, resulting in a significant error. So, its value is usually an integer ranging from 50 to 100. $S(\omega_i)$ is the spectrum of irregular waves.

The Jonswap spectrum is a wave spectrum model based on a series of extensive measurements in the British North Sea and is the most commonly used wave spectrum in the field of wave energy research [20]. In this paper, an improved Jonswap-type spectrum was adopted, and its formulas are given in Formulas (96) to (99):

$$S(\omega_i) = \alpha H_s^2 \omega_p^4 \omega_i^{-5} e^{-\frac{5}{4}\left(\frac{\omega_i}{\omega_p}\right)^{-4}} \gamma^a \tag{96}$$

$$\alpha = \frac{0.06238(1.094 - 0.01915\ln\gamma)}{0.230 + 0.0336\gamma - 0.185(1.9+\gamma)^{-1}} \tag{97}$$

$$a = e^{-(\omega_i-\omega_p)^2/2\sigma^2\omega_p^2} \tag{98}$$

$$\sigma = \begin{cases} 0.07, \omega_i \le \omega_p \\ 0.09, \omega_i > \omega_p \end{cases} \tag{99}$$

In the formulas, H_s is the effective wave height of waves, ω_p is the peak frequency of waves, and γ is the peak elevation factor, which generally ranges from 1 to 10. Referring to the existing literature and based on the wave conditions in most sea areas, this paper uses a spectral peak elevation factor of $\gamma = 2$.

As shown in Figure 14, the spectrum density function of the Jonswap spectrum with a peak frequency of 3.8 rad/s and an effective wave height of 0.75 m was generated based on the model established in this paper.

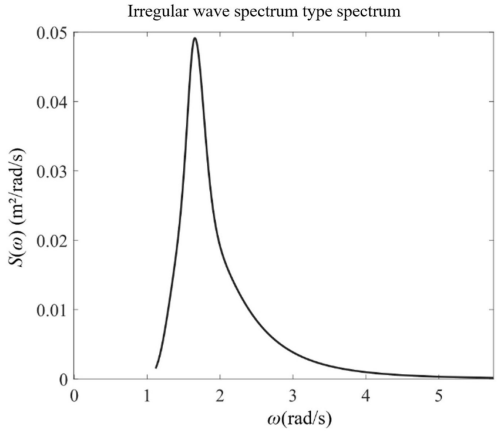


Figure 14. Jonswap spectral density function curve (the peak frequency of the spectrum is 3.8 rad/s).

3.2. Experimental Simulation of Float Motion Under Irregular Waves

In this section, a ground test is conducted to simulate the motion of a floating body input into the wave energy converter under the action of irregular waves. An electric push rod is used to simulate the motion of the float, which pushes the PTO rod to make the wave energy generation device generate electricity. Then, the test output power of the wave power generation device is compared with the calculation results of the time-domain power calculation model. Finally, the accuracy of the model built in this section is verified.

An irregular wave lasting 180 s was generated based on the Jonswap irregular wave spectrum in Section 3.1.2 and related literature data [21]. Based on the frequency-domain calculation model established in Section 2.2 and the time-domain power calculation model established in Section 2.2.4, the time-domain motion response of each float in the hybrid-sized wave energy generation array was computed. The calculation result of one of the floats was selected. The displacement response curve of the selected float is shown in Figure 15a, and the velocity response curve is shown in Figure 15b. The calculated float velocity was imported into the program code in the form of an array. Then, it was used to program the ground test control system, which facilitated communication between the PC and PLC.

The parameters of the screw and disc motors are shown in Table 3. The PC was used as the upper computer, and the USB interface was used to communicate with the PLC controller. The C programming language was used to write programs and then modify variable values in the network registers of the PLC in real time. Therefore, in this section, the PC was programmed in C language as the upper computer. Based on the

speed response of the float under irregular waves, which was obtained using the frequency-domain calculation model established in Section 2.2.2 and the time-domain calculation model established in Section 2.2.3, the variable value in the network register for controlling the speed of the electric push rod in the PLC was modified in real time to simulate the speed response of the float under irregular waves using the electric push rod.

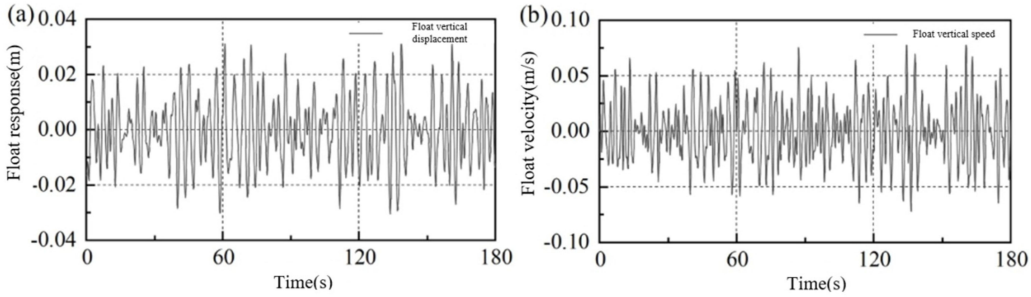


Figure 15. Wave height and wave velocity: (**a**) Wave height; (**b**) Wave velocity.

Table 3. Parameters of the disc motor and screw.

Name of Parameter	Numerical Value
Rated power	200 W
Stator resistance	3.5 Ω
Iss inductance	3.28 Hm
Motor flux linkage	0.22 Wb
Number of pole pairs	2
Rotational inertia	0.00325 kg·m^2
Lead screw length/Length of thread	240 mm/205 mm
Lead of the lead screw/Lead angle	5 mm/10°
Diameter of axle/Lead screw outside diameter	12 mm/16 mm

3.3. Comparison of Simulation Test Results

Figure 16 shows the process chart of the ground equivalent simulation test. The PC ran the written C language code as the upper computer, communicating with the PLC. The code controlled the electric push rod to simulate the float's input to the wave energy converter under the action of irregular waves and pushed the PTO rod of the power generation device prototype, causing it to make reciprocating linear motion. The power generation device generated electric energy, and the externally connected load light bulb shone. The oscilloscopes connected to both ends of the bulb displayed the changes in voltage at both ends of the load, and the faster the movement of the push rod, the greater the voltage generated by the prototype device, and the higher the brightness of the bulb, as shown in Figure 16a,b. The oscilloscope saved the waveform and data of the voltage for subsequent data processing.

Under the action of irregular waves, the load power data obtained using the time-domain model and the load power data measured during the ground test were collected. Because the denominator was too small when the power parameter was small, this led to a large calculation error. In order to better evaluate the model's effectiveness, this paper adopted the following formulas for the maximum error and average error [22]:

$$Ers = \frac{\sum_{i=1}^{N} |S'(t) - S(t)|}{\sum_{i=1}^{N} |S(t)|} \tag{100}$$

$$Er\max = \frac{\max|S'(t) - S(t)|}{\frac{\sum_{i=1}^{N}|S(t)|}{N}} \quad (101)$$

The results obtained from the calculation model at time t correspond to $S(t)$, the test measurement results at time t correspond to $S'(t)$, N is the total number of data points in this group. The calculation result of Formula (100) was named the average error, and the calculation result of Formula (101) was named the maximum error.

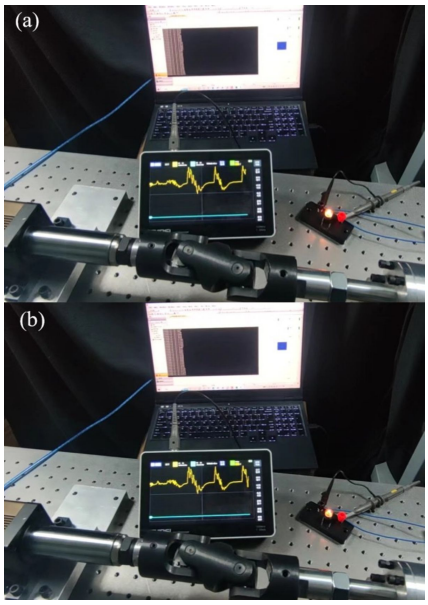


Figure 16. Experimental process: (**a**) The small bulb is relatively bright; (**b**) The small bulb is relatively dim.

As shown in Figure 15, the response curve of the float over 180 s is divided into four time periods: a short time period (one peak), an ebb-tide period, a flood-tide period, and a long time period. The analysis below is based on this grouping.

First, based on the calculation model and test data, a comparison diagram of the calculation results of the intra-peak time-domain model and the ground test results was created. The results are shown in Figure 17. It can be seen from the curve data in Figure 17a,b that the average errors between the model established in this paper and the results obtained from the ground tests were 0.077 and 0.058, respectively, and the maximum errors were 0.701 and 0.428, respectively. It can be seen that the maximum error in Figure 17a occurred at about 6.95 s, and that the maximum error in Figure 17b occurred at about 13.52 s. This was mainly caused by the fact that the experimental platform had just been started, the motor and other equipment had not reached dynamic balance, and the motor speed fluctuated. At the same time, because the experimenter needed to check the operating status of the equipment in the initial stage and walked back and forth, this led to the vibration of the testing equipment and produced errors. However, since the cumulative action time was less than 0.03 s and the two curves exhibited good agreement in other time periods, it can be concluded that this calculation model ensures the accuracy of the results over a short time period.

Then, based on the calculation model and test data, a comparison diagram of the calculation results of the time-domain model and the ground test results at the three peaks was created for the ebb-tide period. The results are shown in Figure 18. It can be seen from the curve data that the average error between the model established in this paper and the results obtained from the ground tests was 0.080, and the maximum error was 0.791. It can be seen that the error reached its maximum at about 42.26 s. This error was mainly

caused by the vibration of the equipment and instruments. These vibrations significantly affected the incident water flow. As the energy of the ocean current gradually decreased at low tide, the fluctuations of the three peaks gradually decreased with decreasing power. Since the motor had reached dynamic balance at this time, the average error obtained was smaller than that shown in Figure 17. However, since the cumulative action time was less than 0.05 s and the two curves exhibited good agreement in other time periods, it can be concluded that this calculation model ensures the accuracy of the results during the ebb-tide period.

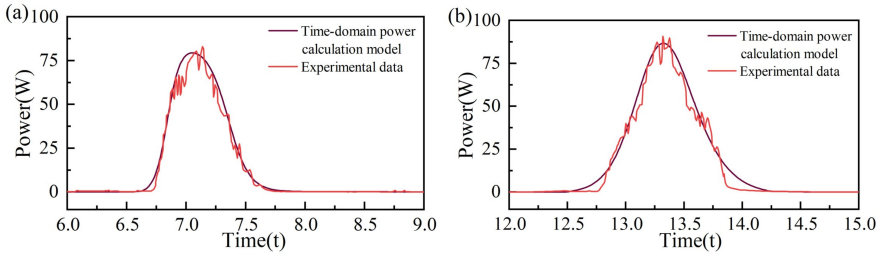


Figure 17. Comparison between the data obtained from the time-domain model at a peak and the data obtained from the experiment: (**a**) the peak of 6.0 s to 9.0 s; (**b**) The peak of 12.0 s to 15.0 s.

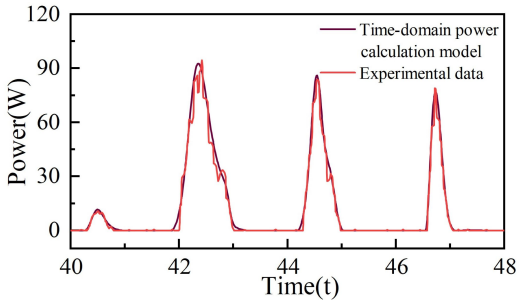


Figure 18. Comparison between data obtained from the time-domain power calculation model and data obtained from the test during the ebb-tide period.

Then, based on the calculation model and test data, a comparison diagram of the calculation results of the time-domain model and the ground test results at the three peaks was created for the flood-tide period. The results are shown in Figure 19. It can be seen from the curve data that the average error between the model established in this paper and the results obtained from the ground tests was 0.037, and the maximum error was 0.543. It can be seen that the error reached its maximum at about 86.35 s. At about 86.3 s, the vibration frequency of the float caused by the ocean current may have matched the natural frequency of the data collector's support frame, leading to resonance, which interfered with the normal work of the data collector and produced the maximum error. However, since the maximum error was still less than 0.6 and the cumulative action time was less than 0.03 s, it had little impact on the overall calculation. Since the two curves exhibited good agreement in other time periods, it can be concluded that this calculation model ensures the accuracy of the results during the flood-tide period.

Finally, based on the calculation model and test data over a long time period, a comparison diagram of the calculation results of the time-domain power calculation model and the ground test results for random ocean currents was created. The results are shown in Figure 20. It can be seen from the curve data that the average error between the results obtained from the model established in this paper and the ground test results was 0.006, and the maximum error was 0.848. It can be seen that the error reached its maximum at about 128.59 s. This error was caused by the disturbance of the site environment and the vibration of other equipment, which could not be avoided because of the long time

period. However, since the cumulative action time was less than 0.01 s and the two curves exhibited good agreement in other time periods, it can be concluded that this calculation model ensures the accuracy of the results over a long time period.

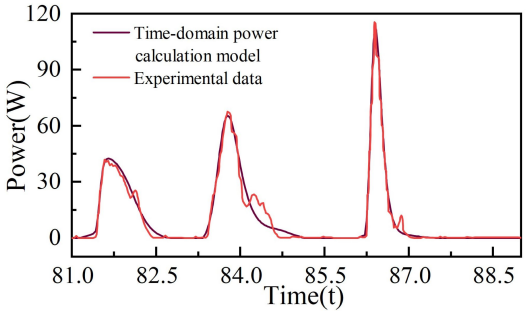


Figure 19. Comparison between data obtained from the time-domain power calculation model and data obtained from the test during the flood-tide period.

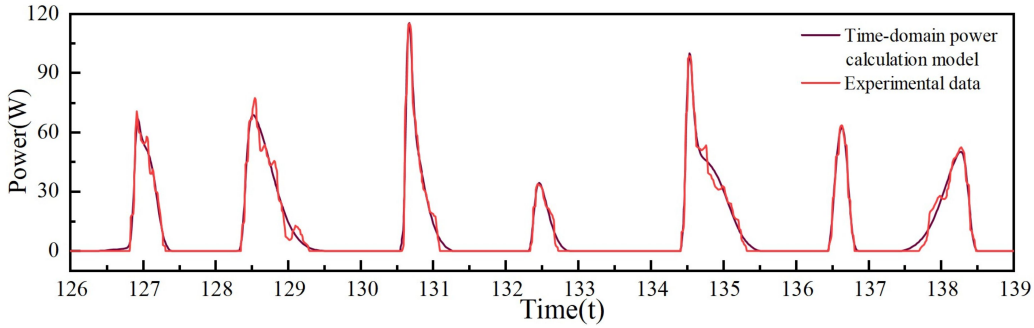


Figure 20. Comparison between data obtained from the time-domain power calculation model and test data over a long period of time.

As can be seen from the curve and the above analysis, the results of the time-domain power calculation model established in this section not only fit well with the experimental results over a short time period but also reflect the changing trend of the load power at ebb tide, at flood tide, and over a long time period. As shown in Table 4, the overall average error of the fitting results was 0.052, which is small.

Table 4. The error between the calculated model results of a single float and the equivalent experimental results on the ground.

Project Name	Maximum Error (Cumulative Action Time)	Average Error
Comparison of results within a peak a	0.701 (0.02s)	0.077
Comparison of results within a peak b	0.428 (0.03s)	0.058
Comparison of results at low tide stage	0.791 (0.05s)	0.080
Comparison of results at high tide stage	0.543 (0.03s)	0.037
Comparison of long-term results	0.848 (0.01s)	0.006
Overall average error 0.052		

Because the setting of the incident water is based on the hydrodynamic model established in this paper, the experimental data of the other three floats were obtained by changing the incident water for the experiments. Based on the calculation model established in this paper, the theoretical data of the other three floats were obtained. The total output power of the array was a simple sum of the output power of the power generation device connected to each float. The theoretical data and experimental data of the power generation array were obtained by adding the data from the other three floats to the data from this

float. The average error of the array was obtained. As shown in Table 5, the average error of the whole array was 0.044.

Table 5. The error between the calculated model results of each float and the equivalent experimental results on the ground.

Project Name	Average Error
Float 1	0.052
Float 2	0.048
Float 3	0.036
Float 4	0.040
Average error of the whole array 0.044	

In order to analyze the sensitivity of the average error of the whole array, three control groups were established in this experiment. Keeping other experimental conditions unchanged, we adjusted the peak frequency of the water spectrum, the height of the water wave, and the noise of the experimental site each by 10%. By analyzing the data from these three experimental settings, we obtained their average error ranges, as shown in Figure 21. Among these, the average error due to changes in water wave height fluctuated the most, ranging from 0.036 to 0.062. It can be concluded that the average error was most sensitive to the change in water wave height.

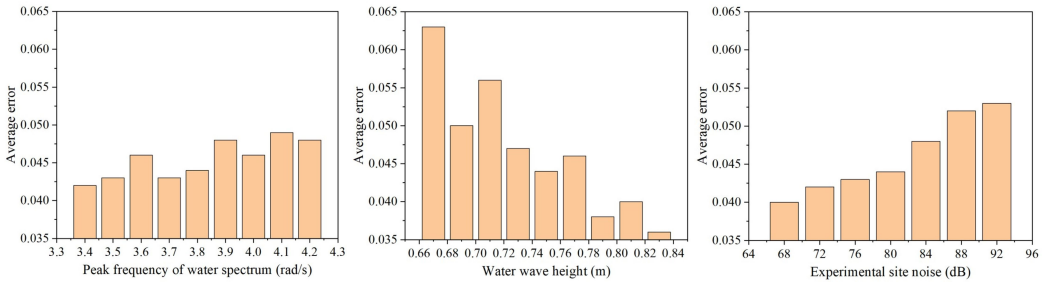


Figure 21. Sensitivity analysis of average errors.

Using Abdulkadir's algorithm [9], under the same incident water flow conditions, the data obtained using the traditional calculation model with the same float size were obtained. From this, the error of the traditional calculation model was determined, as shown in Table 6. The maximum error of the traditional calculation model was 0.983, and the average error was 0.162, which is much higher than that of the time-domain power calculation model.

Table 6. Comparison of calculation errors between the time-domain power calculation model and the traditional calculation model.

Model	Maximum Error (Cumulative Action Time)	Average Error
Time-domain power calculation model	0.848	0.044
Traditional calculation model	0.983	0.162

In the above experimental results, we can see that the error of the model established in this paper was well below 10% across all conditions. Therefore, the model established in this chapter accurately reflected the output power of a mixed-size wave power generation platform array under the action of irregular waves in the time domain. In addition, it can be seen from the test data that the output power of the power generation device exhibited certain fluctuations in local areas, but overall, the prototype did not experience excessively

low or no output power under the action of irregular waves and was able to achieve continuous power output.

In this section, an irregular wave model was established to set the incident water flow conditions, and then, based on the hydrodynamic model and calculation model established above, the frequency-domain response and time-domain response of floats in the array under irregular incident waves were obtained. Then, the velocity responses of the floats under the action of irregular waves were simulated through experiments. Then, the calculation results of the model were compared with the experimental results. Then, the data from the four floats were aggregated to obtain the data for the whole array, and the calculation error of the whole array was compared with that of the traditional model, verifying the effectiveness of the time-domain power calculation model of the array established in this paper.

4. Conclusions

Compared with traditional array configurations with the same float sizes, the hybrid array has higher output power. However, the frequency-domain hydrodynamic modeling of existing hybrid arrays does not consider the differences from traditional array configurations. At the same time, existing research indicators cannot directly reflect the power generated by the array in the time domain, and the research scheme does not fully consider factors affecting the output power of the array, which leads to inaccurate calculation results of the output power of the hybrid array. To address the above problems, this paper corrected the boundary integral equation for the floating bodies in the array by considering the water depth condition of Green's function and corrected the frequency-domain response equation for the floating bodies in the array by considering the viscous effect of the relatively small floating bodies in the array. Based on this, a frequency-domain hydrodynamic model of the hybrid array was constructed, providing a theoretical basis for the establishment of the calculation model. An oscillating float-type wave energy converter was designed and developed, and the PTO system and motor of the device were modeled in the time domain. Using the inverse Fourier transform, the frequency-domain hydrodynamic model of the hybrid-sized wave energy generation array was converted into the time domain, and finally, the time-domain power calculation model of the hybrid-sized wave energy generation array was obtained. Based on the established model, simulations and experimental analyses were carried out, and a ground test platform was built. The effectiveness of the model was verified through comparative tests and model calculation results.

Author Contributions: Formal analysis, Y.Z.; Investigation, A.F.; Methodology, H.Z.; Supervision, J.Y.; Writing—original draft, A.F.; Writing—review and editing, A.F., H.Z., Y.Z. and J.L. All authors have read and agreed to the published version of the manuscript.

Funding: This research was funded by the National Natural Science Foundation of China (Grant Nos. U21B2075 and 52475249), the National Key R&D Program of China (Grant Nos. 2023YFC2205900, 2023YFC2205903, and 2023YFC2205904), the Reusable Space Debris Capture and Removal Project (Grant No. KJSP2020010302), the Stable Supporting Fund of National Key Laboratory of Underwater Acoustic Technology (Grant No. JCKYS2023604SSJS012), the Fundamental Research Funds for the Central Universities (Grant No. 3072023WD070101), and the National Natural Science Foundation of China (Grant No. 52375025).

Institutional Review Board Statement: Not applicable.

Informed Consent Statement: Not applicable.

Data Availability Statement: Due to privacy restrictions, the data are not publicly available.

Acknowledgments: The authors would like to thank the College of Mechanical and Electrical Engineering at Harbin Engineering University for their financial support and provision of equipment for this project.

Conflicts of Interest: The authors declare no conflicts of interest.

References

1. Bechlenberg, A.; Wei, Y.; Jayawardhana, B.; Vakis, A.I. Analysing the influence of power take-off adaptability on the power extraction of dense wave energy converter arrays. *Renew. Energy* **2023**, *211*, 1–12. [CrossRef]
2. Mary, G. Multi-parameter optimization of hybrid arrays of point absorber wave energy converters. In Proceedings of the 12th European Wave and Tidal Energy Conference, Cork, Ireland, 27–31 August 2017; pp. 26–37.
3. Sinha, A.; Karmakar, D.; Soares, C.G. Performance of optimally tuned arrays of heaving point absorbers. *Renew. Energy* **2016**, *92*, 517–531. [CrossRef]
4. Giassi, M.; Castellucci, V.; Goteman, M. Economical layout optimization of wave energy parks clustered in electrical subsystems. *Appl. Ocean Res.* **2020**, *101*, 102274. [CrossRef]
5. Kara, F. Effects of a vertical wall on wave power absorption with wave energy converters arrays. *Renew. Energy* **2022**, *196*, 812–823. [CrossRef]
6. Li, M.; Jia, G.; Mahmoud, H.; Yu, Y.H.; Tom, N. Physics-constrained Gaussian process model for prediction of hydrodynamic interactions between wave energy converters in an array. *Appl. Math. Model.* **2023**, *119*, 465–485. [CrossRef]
7. Göteman, M.; Engström, J.; Eriksson, M.; Isberg, J.; Leijon, M. Methods of reducing power fluctuations in wave energy parks. *J. Renew. Sustain. Energy* **2014**, *6*, 043103. [CrossRef]
8. Sun, P.Y. Sensitivity analysis of geometric characteristics on the cavity-buoy for energy capture efficiency enhancement of a semi-submersible floating-array-buoy wave energy converter system. *Ocean Eng.* **2024**, *294*, 116735. [CrossRef]
9. Abdulkadir, H.; Abdelkhalik, O. Optimization of heterogeneous arrays of wave energy converters. *Ocean Eng.* **2023**, *272*, 113818. [CrossRef]
10. Goteman, M. Wave energy parks with point-absorbers of different dimensions. *J. Fluids Struct.* **2017**, *74*, 142–157. [CrossRef]
11. Mclver, P. Some hydrodynamic coefficients in heave of two concentric surface-piercing truncated circular cylinders. *Appl. Ocean Res.* **1994**, *19*, 283–291.
12. Göteman, M.; Engström, J.; Eriksson, M.; Isberg, J. Fast modeling of large wave energy farms using interaction distance cut-off. *Energies* **2015**, *8*, 13741–13757. [CrossRef]
13. Snieder, R.; Huub, D.; Vasconcelos, I. Extracting the Green's function from measurements of the energy flux. *J. Acoust. Soc. Am.* **2012**, *131.4*, EL309–EL315. [CrossRef] [PubMed]
14. Li, Y. *Effects of Waves on Offshore Buildings*, 3rd ed.; Ocean Press: Beijing, China, 2015; pp. 35–42.
15. Xu, J.; Zhao, Y.; Zhan, Y.; Yang, Y. Maximum power point tracking control for mechanical rectification wave energy converter. *IET Renew. Power Gener.* **2021**, *15*, 3138–3150. [CrossRef]
16. Son, D.; Belissen, V.; Yeung, R.W. Performance validation and optimization of a dual coaxial-cylinder ocean-wave energy extractor. *Renew. Energy* **2016**, *92*, 192–201. [CrossRef]
17. Wu, S.; Liu, Y.; Qin, J. Experimental analyses of two-body wave energy converters with hydraulic power take-off damping in regular and irregular waves. *Renew. Power Gener.* **2021**, *15*, 3165–3175. [CrossRef]
18. Falnes, J. *Ocean Waves and Oscillating Systems*; Cambridge University Press: Cambridge, UK, 2002; pp. 43–57.
19. Nie, Z.; Xiao, X. Emulation and control methods for driect drive linear wave energy converters. *IEEE Trans. Ind. Inform.* **2013**, *9*, 790–798. [CrossRef]
20. Deng, F.; Wang, J.; Wang, J. Estimation of a five-parameter JONSWAP spectra with an improved particle swarm optimization. *Appl. Ocean Res.* **2023**, *136*, 103580. [CrossRef]
21. Yin, H.; Cai, F.; Qi, H.; Jiang, Y.; Liu, G.; Cao, Z.; Sun, Y.; Xiao, Z. Analysis of Tidal Cycle Wave Breaking Distribution Characteristics on a Low-Tide Terrace Beach Using Video Imagery Segmentation. *Remote Sens.* **2024**, *16*, 4616. [CrossRef]
22. Zhou, Y.J. A Study on Integral Algorithm for Acceleration Test to Get Displacement and Application. Master's Thesis, Chongqing University, Chongqing, China, 2013. (In Chinese)

Disclaimer/Publisher's Note: The statements, opinions and data contained in all publications are solely those of the individual author(s) and contributor(s) and not of MDPI and/or the editor(s). MDPI and/or the editor(s) disclaim responsibility for any injury to people or property resulting from any ideas, methods, instructions or products referred to in the content.